

Performance of OLCI Sentinel-3A satellite in the Northeast Pacific coastal waters



Fernanda Giannini ^{a,b,c,*}, Brian P.V. Hunt ^{b,c,d}, Derek Jacoby ^e, Maycira Costa ^a

^a Department of Geography, University of Victoria, PO Box 1700 STN CSC, Victoria, BC V8W2Y2, Canada

^b Institute for the Oceans and Fisheries, University of British Columbia, AERL, 2202 Main Mall, Vancouver, BC V6T1Z4, Canada

^c Hakai Institute, PO Box 309, Heriot Bay, BC V0P1H0, Canada

^d Department of Earth, Ocean and Atmospheric Sciences, University of British Columbia, 2020 –2207 Main Mall, Vancouver, BC V6T1Z4, Canada

^e Department of Computer Science, University of Victoria, PO Box 1700 STN CSC, Victoria, BC V8W2Y2, Canada

ARTICLE INFO

Keywords:

Ocean colour
OLCI Sentinel-3A
Remote sensing of coastal waters
Northeast Pacific coast

ABSTRACT

Coastal oceans play a pivotal role in fisheries production and global biogeochemical cycles, making large-scale monitoring an essential task. The advent of modern remote sensors, such as OLCI (Ocean Land Colour Instrument), on board the Sentinel-3A satellite, has made it possible to obtain oceanic biogeochemical products at higher spatial (300 m) and temporal (daily) resolutions than previously possible. However, validating the Sentinel-3A retrievals for coastal waters is an ongoing effort. Using a regional *in situ* dataset from British Columbia (BC) and Southeast Alaska (SEA) coastal waters, we evaluated the performance of OLCI Sentinel-3A in retrieving remote-sensing reflectance (R_{rs}) and biophysical products, including total suspended matter (TSM), chlorophyll-a concentration (Chl-a) and coloured dissolved organic matter (CDOM). The OLCI data were processed through a spectral optimization-based algorithm (POLYMER) and a neural net-based (NN) algorithm (C2RCC), including the original (C2RCC v1) and the alternative version (altNN or v2), in which the neural network was trained with extended ranges to cope with larger dynamic range for high backscatter waters. The processors' performance was evaluated through match-up analysis using data from southern BC, as well as expected ranges and seasonal trends for northern BC and SEA. Multimetric statistical analyses demonstrated that POLYMER provided the best overall performance for TSM and Chl-a retrievals, with the Chl-a product improved by the use of the so-called "Case-2" flag. Despite the relative outperformance of POLYMER-derived products, with low systematic biases, the relative percent differences are still high (80–100%) and should be acknowledged in future analyses when using these data. CDOM, only retrieved here from NN approaches, was better estimated using the alternative version of C2RCC. The best performing approaches were used to evaluate Level-3 composites for northern BC and SEA waters. The observed spatial and seasonal trends compared favourably with those reported in the literature, including highlighting more productive areas (e.g. west coast of Vancouver Island), and the important interactions between riverine systems and adjacent coastal waters (e.g., high TSM and CDOM loads near the Skeena and Nass rivers). This study demonstrated the benefits of OLCI Sentinel-3A to investigate complex coastal ecosystems and provides a robust evaluation of OLCI performance and a framework for future observational and process-oriented studies.

1. Introduction

Remotely sensed data of the oceans' surface have been increasingly used to monitor and understand biogeochemical processes that might influence or be associated with the changes in the Earth's climate (Behrenfeld et al., 2006; Behrenfeld et al., 2016; Sathyendranath et al.,

2017; Dutkiewicz et al., 2019). Since the launch of the NASA Coastal Zone Colour Scanner (CZCS) on board the Nimbus-7 in 1978, ocean colour sensors have been used to provide biogeophysical and water quality parameters at higher spatial and temporal resolution compared to the field data (McClain, 2009; Groom et al., 2019). Satellite retrievals include chlorophyll-a concentration (a proxy for phytoplankton

* Corresponding author at: Universidade Federal do Rio Grande (FURG), Laboratório de Fitoplâncton e Microorganismos Marinhos - Instituto de Oceanografia, 96203-900 Rio Grande, RS, Brazil.

E-mail address: giannini@furg.br (F. Giannini).

biomass; e.g., Mélin et al., 2011; Lavender et al., 2015), load and sources of dissolved organic material (e.g., Nelson and Siegel, 2013; Mannino et al., 2014), and levels of turbidity and sediment transport (e.g., Nechad et al., 2010; Dogliotti et al., 2015). However, to date, ocean colour remote sensing has most effectively been applied in off-shelf waters, while its application in coastal waters remains challenging, inhibiting the retrieval of accurate satellite-derived products (IOCCG, 2000; Park and Ruddick, 2005; Werdell et al., 2018).

Optically, coastal waters differ from the open ocean due to the presence of non-algal particles and dissolved material, in addition to the phytoplankton cells, which together interact with (*i.e.*, absorb and scatter) the incident light in the ocean (Prieur and Sathyendranath, 1981). The concurrent presence of several optically active constituents modulates the reflectance signal leaving the surface water and detected by remote sensors, which is ultimately used to inversely derive products through bio-optical models (Mobley, 1994; Morel and Maritorena, 2001). Thus, in coastal waters, especially when turbid freshwater outflows are present, the development of coastal bio-optical models, as well as regional validation of existing models, is required and has indeed been performed by a number of research groups worldwide (e.g., Moore et al., 1999; Nechad et al., 2010; Giannini et al., 2013; Tilstone et al., 2017; Carswell et al., 2017). Furthermore, quantifying the parameters required for the removal of the atmospheric signals from the top of the atmosphere radiance data measured by satellite-borne sensors is more complex for turbid coastal waters than for oceanic waters (Siegel et al., 2000), affecting the performance of atmospheric correction models. In clear waters, the assumption that seawater is totally absorbent in the near-infrared (NIR) spectral bands is accepted, and the aerosol optical properties are then modelled for the visible bands (Gordon and Wang, 1994). However, this assumption is invalid in turbid or non-phytoplankton-dominated waters (Ruddick et al., 2000; Goyens et al., 2013), and the aerosol content in the atmosphere is rather inferred from signals in the NIR or the short-wavelength infrared region (SWIR) or a combination of SWIR/NIR (Wang and Shi, 2005; Ruddick et al., 2000; Carswell et al., 2017). Alternatively, atmospheric correction algorithms have been developed based on iterative coupled ocean-atmosphere models, such as POLYMER (POLYNomial based algorithm applied to MERIS), based on polynomial spectral matching technique (Steinmetz et al., 2011) and C2RCC (Case-2 Regional Coast Colour), based on artificial neural network simulations (Doerffer and Schiller, 2007; Brockmann et al., 2016). Further details about the ocean-atmosphere coupled models are provided in Section 2.3.

Beyond their optical complexity, coastal environments can have a high degree of geomorphological and oceanographic complexity due to small-scale dynamic processes such as tidal cycles, riverine discharge and frontal systems, and capturing these dynamics requires satellite data at fine spatial (few meters) and temporal (hours to daily) resolutions (IOCCG, 2000). Therefore, in addition to the development of bio-optical and atmospheric correction models tuned to coastal conditions, instrument-related advances have tended towards sensors capable of dealing with optically and oceanographically complex waters. One such advancement is the OLCI sensor, part of the Sentinel-3 mission jointly operated by ESA and EUMETSAT, which has been operational since April 2016. The Sentinel-3 OLCI delivers data from the surface ocean at 300 m resolution and was designed to continue the Envisat MERIS mission. The OLCI sensor has an improved signal-to-noise ratio and off-nadir swath centered to minimize sun glint (Donlon et al., 2012). Sentinel-3 OLCI is therefore particularly well suited to studies of complex nearshore waters, with potential applications in both research and management.

A critical first step before the broader application of OLCI Sentinel-3 is the validation of target products. Indeed, since its launch, OLCI's performance and associated uncertainties have been under continuous evaluation, especially for coastal waters (e.g., Hieronymi et al., 2017; Zibordi et al., 2018; Mograne et al., 2019; Gossn et al., 2019). However, due to its relatively recent launch, there is still extensive discussion

about the deviations found by the different processing approaches applied to Sentinel-3A OLCI imagery, and consequently derived products. The aim of this study was to evaluate the performance of this sensor to retrieve biogeophysical products (chlorophyll-a concentration, total suspended material, and coloured dissolved organic matter) in the optically complex coastal waters of British Columbia (BC, Canada) and Southeast Alaska (SEA, US). The satellite-derived products were generated through different atmospheric correction approaches, and their performances were statistically validated against *in situ* data. In addition, in order to evaluate the application of the methods for large-scale imagery of the Northeast Pacific coastal waters, the retrieved data were discussed in terms of expected seasonal and latitudinal dynamics for the study area.

2. Methods

2.1. Study area

The study was conducted in the Northeast Pacific, encompassing coastal waters of British Columbia (CA; 47°N to 54.7°N) and Southeast Alaska (US; 54.7°N to 59°N) (Fig. 1). The region presents complex geomorphological and bathymetric structure (Thomson, 1981; O'Neil et al., 2015), influenced by dynamic oceanographic processes (e.g., upwelling/downwelling systems; Pawlowicz, 2017), and is subject to seasonally high biological productivity (Ware and Thomson, 2005; Malick et al., 2015). The coastal ocean receives the input of massive freshwater discharges from a large network of forested watersheds (Royer, 1982; Morrison et al., 2012) that belongs to the Pacific Coastal Temperate Rainforest (PCTR) domain (O'Neil et al., 2015; McNicol et al., 2019). The discharge transports substantial amounts of terrestrial organic and inorganic material (Oliver et al., 2017; McNicol et al., 2019), and this is expected to significantly affect bio-optical properties (Loos and Costa, 2010; Phillips and Costa, 2017) and biogeochemical cycles (Masson and Peña, 2009; Suchy et al., 2019) of the coastal margins.

Several studies have optically characterized the southern BC coast, with most of the studies carried out within the Strait of Georgia (SoG) (Komick et al., 2009; Loos and Costa, 2010; Phillips and Costa, 2017). The SoG waters are mainly influenced by the dynamics of the Fraser River plume, where rapid light attenuation occurs due to backscatter from inorganic particles and high loads of dissolved organic material, especially in the spring and summer (e.g., Loos and Costa, 2010; Carswell et al., 2017; Phillips and Costa, 2017). Despite the challenges associated with remote sensing of coastal waters (Ruddick et al., 2000; Goyens et al., 2013) and the use of coarse spatial resolution (1 km or lower), previous studies using satellite data have been able to identify important biogeochemical dynamics and seasonality in the region (e.g., Ware and Thomson, 2005; Jackson et al., 2015; Malick et al., 2015; Suchy et al., 2019). Using MODIS-Aqua with a regional atmospheric correction approach (*i.e.*, Carswell et al., 2017), Suchy et al. (2019) demonstrated that the dynamics of phytoplankton biomass in the central SoG is controlled by local environmental drivers, including the Fraser River discharge and its impact on water column stratification, while large-scale climate indices strongly influence the northern SoG. On a broader spatial scale, *i.e.*, including Central and Northern BC and the Southeast Alaska coast, phytoplankton biomass and bloom timing vary spatially and interannually, with higher biomass and earlier blooms observed in the southern BC coast, *i.e.*, in the SoG, followed by the southwest coast of Vancouver Island (Jackson et al., 2015). In addition, combining satellite-derived chlorophyll and pink salmon recruitment data, Malick et al. (2015) showed that the bloom timing has a larger impact on the stock productivity of this coastal region than the magnitude of phytoplankton biomass.

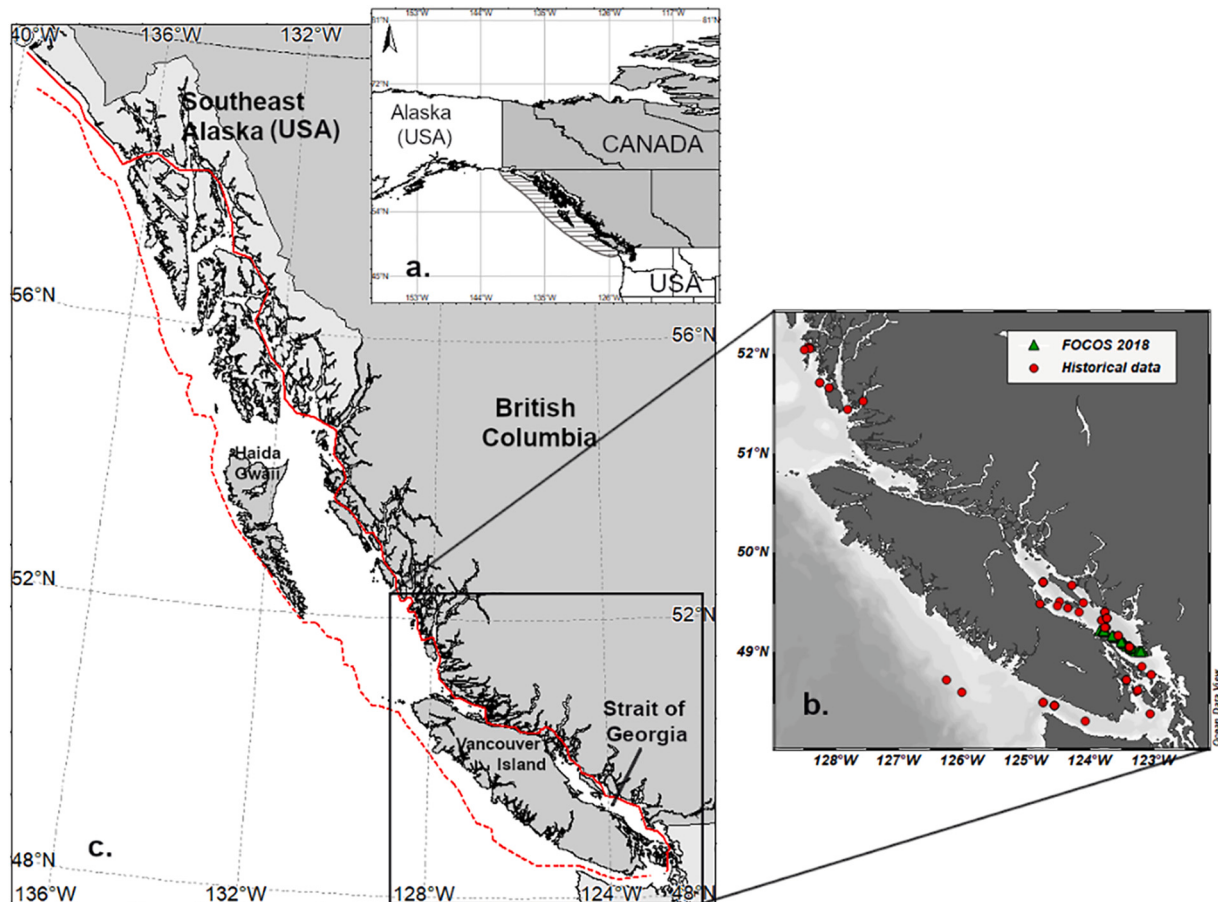


Fig. 1. (a) Study region along the Northeast Pacific Ocean. The dashed area indicates the outer boundary of the region of interest along British Columbia (BC) and Southeast Alaska (SEA) coastal waters. (b) Field sampling stations concentrated in BC, including historical data from the Hakai Institute and DFO (Chl-a) and recently collected data (Rrs, Chl-a, TSM and CDOM data). (c) Transect lines used to extract Level-3 OLCI data from nearshore (solid line) and continental shelf, over the 800 m isobath (dashed line).

2.2. In situ data collection

In situ data were obtained through the research program FOCOS (Ferry Ocean Colour Observation Systems) from March to August 2018, onboard the BC ferry “Queen of Alberni” in a transect along the central Strait of Georgia (Fig. 1b). Water samples were obtained from a flow-through system, with an intake depth of about 1–2 m. Additional data were obtained from publicly available databases from Fisheries and Oceans Canada (DFO) and Hakai Institute (April 2016 to March 2018). Although the field data were constrained to BC Southern and Central coasts (Fig. 1b), they represent optically contrasting conditions expected in BC and SEA coastal waters.

2.2.1. Total Suspended Material (TSM)

Approximately 1.5 L of seawater was filtered onto pre-weighed 0.7 µm GF/F filters to determine TSM (mg/L) using the gravimetric method (Pearlman et al., 1995). Filters were pre-washed and pre-weighed, and were rinsed with deionized (DI) water after sample filtration to avoid sea salt retention, following the protocols described by Stavn et al. (2009) and Röttgers et al. (2014). Final TSM concentrations are averages of triplicates, with a coefficient of variation (CV) < 25%.

2.2.2. Chlorophyll-a concentration (Chl-a)

Two different protocols were used to measure the *in situ* Chl-a concentration:

(i). Historical dataset (DFO and Hakai; 2016–2018): seawater samples were filtered onto 25 mm GF/F filters and stored in glass scintillation vials at -20 °C prior to analysis. Pigments were subsequently extracted in 90% acetone at -20 °C for 24 h. DFO samples were analyzed on a Turner 10 AU fluorometer and Hakai samples on a Turner Design Trilogy fluorometer, both calibrated with a commercial pure Chl-a standard. Fluorescence readings taken before and after acidification were used to calculate chlorophyll-a and phaeopigment concentrations (Holm-Hansen et al., 1965); DFO data are averages from duplicates, with CV < 30%. Hakai data are not duplicates but passed through a rigorous quality control procedure.

(ii). BC ferry (FOCOS program): seawater samples were immediately frozen after filtration and stored at -80 °C until extraction and analysis on a Shimadzu HPLC with a unique combination of both monomeric and polymeric C18 columns combined with a variable flow binary (Pinckney, 2010). Chl-a represents the chlorophyll-a + chlorophyllide-a + chl-a' (isomer) and chl-a allomers. HPLC samples were not collected in duplicate, however, the data agreed well with paired fluorometric analysis ($R^2=0.81$; $\text{Chla}_{\text{HPLC}} = 0.83\text{Chla}_{\text{fluor}} + 0.75$).

2.2.3. Absorption by Coloured Dissolved Organic Matter (CDOM)

GF/F filtrates were re-filtered onto 0.2 µm membrane filters and collected in previously acid cleaned and sterilized bottles and kept in the dark at 4 °C until analysis within 24 h. The spectral absorbance of the dissolved material was measured between 300 and 750 nm on a

USB4000 Ocean Optic spectrophotometer. CDOM absorbance spectra measurements were blank-corrected, using freshly produced DI water as the reference, and a baseline correction was applied at 715 nm, assuming negligible CDOM absorption at that wavelength (Mitchell et al., 2002). CDOM absorbance was further converted into absorption coefficient, $a_{CDOM}(\lambda)$ in m^{-1} according to the following equation:

$$a_{CDOM}(\lambda) = \frac{2.303^*A(\lambda)}{L} \quad (1)$$

where $A(\lambda)$ is the spectral absorbance and L is the cuvette path length in meters. $a_{CDOM}(\lambda)$ data were fitted assuming an exponential decay towards the longer wavelengths (Bricaud et al., 1981), and the magnitude of CDOM content was defined at 443 nm, $a_{CDOM}(443)$, hereafter named CDOM for simplicity. The final results are averages of triplicates, with $\text{CV} < 25\%$.

2.2.4. Above-water radiometry: remote sensing reflectance (Rrs)

A set of hyperspectral radiometers is currently installed on the same BC ferry “Queen of Alberni”, from which the water sampling was carried out. The system measures radiance and irradiance with solar tracking capability that permits autonomous operation (SAS Solar Tracker; SAS-ST) and consists of two hyperspectral radiometers to measure sea surface radiance ($Lt(\lambda)$) and sky radiance ($Li(\lambda)$), and a third sensor to measure total irradiance, ($Es(\lambda)$). From these measurements, remote sensing reflectance, $Rrs(\lambda)$, was derived following Mobley (1999) and subjected to the Spectral Response Function (SRF) according to OLCI Sentinel-3 instrument's spectral characterization. The SAS-ST was configured to avoid infrastructure, shadows, spray, and sun glint (Wang and Costa, 2018), and was fully calibrated by the manufacturer (Satlantic, Inc.) before deployment in 2018. Specifically, $Lt(\lambda)$ and $Li(\lambda)$ were at a fixed viewing zenith angle, $\theta_v = 45^\circ$, and viewing-sun azimuth, $\phi_v = 120^\circ$, to avoid the effects of glint (Hooker and Morel, 2003). The ideal ϕ_v was maintained using an autonomous stepper motor platform that triggered the required positioning according to the ship heading and sun azimuth (Satlantic Inc.). Data from SAS-ST were processed with PySciDON (Python Scientific framework for Development of Ocean Network applications; Vandenberg et al., 2017). The SAS-ST data were acquired every 2 s and binned into 10 s intervals during the processing. For each field station, 80 s averages were used to correspond to the 3×3 pixel window along-track (~ 900 m length), considering the navigation speed, and the *in situ* Rrs dataset presented $\text{CV} < 25\%$. Given the different approaches currently considered for the evaluated processors, i.e., C2RCC (SNAP processing and L2-OCNN) with no BRDF correction and POLYMER with BRDF correction (Park and Ruddick, 2005) (Section 2.3), the SAS-ST data were not BRDF corrected (see Section 4.2).

2.3. Satellite data and algorithms

OLCI Sentinel-3A Level-1 and Level-2 Full-Resolution data were downloaded from the Sentinel-3 Marine CODA (Copernicus Online Data Access) Web Service (data previous to November 29th, 2017 were downloaded from the CODArep portal, as recommended by EUMETSAT). OLCI Level-2 images were used to extract Chl-a, TSM and ADG443 (Neural Network approach for complex waters), while Level-1 data were locally processed through C2RCC (version 1), C2RCC altNN (alternative Neural Network, or version 2) and POLYMER (version 4.9) to obtain Rrs , Chl-a, TSM and CDOM. About 46 images contributed to the Chl-a match-up analysis, and 9 images were used for the Rrs , TSM and CDOM match-ups.

2.3.1. EUMETSAT Level-2 operational processor for complex waters (L2-OCNN)

Level-2 operational products (baseline 2.23), which are operated and distributed by EUMETSAT, were used to obtain TSM, Chl-a and ADG443 (absorption by detritus and dissolved organic matter at 443 nm) derived

for complex water applications (OCNN products; EUMETSAT, 2018). The OCNN products are derived from a specific approach for optically complex waters, defined as Alternative AC as opposed to the baseline AC defined for open waters (EUMETSAT, 2018). In the Alternative AC procedure, the Top-of-Atmosphere (TOA) reflectances in 15 bands (400–753 nm, 778, 865 and 1020 nm), corrected for absorbing gases and the smile effect, are used together with wind speed, salinity, temperature, altitude of the water surface and observation geometry to estimate the water-leaving reflectances and atmospheric parameters. The procedure is based on artificial neural networks (NN) with some pre-corrections (Doerffer and Schiller, 2008). For the OCNN products retrievals from OLCI Sentinel-3, the reflectance is not corrected for the BRDF effects (i.e. they are directional reflectance). The water-leaving reflectance is then submitted, along with angular geometry information, to a neural network (NN) inversion procedure to derive the in-water IOPs (Doerffer and Schiller, 2007). The NN is trained with a large table of simulated angle-dependent radiance spectra generated by a forward model built from the HYDROLIGHT code (Mobley, 1994). The IOPs include the three major components of coastal waters, i.e., scattering by particles, absorption by phytoplankton pigments and absorption by dissolved organic matter. A bio-optical model is also used to convert the inherent optical properties (IOP) into the in-water concentrations, such as TSM and Chl-a, which are based on a large data set collected mainly in European waters.

The NN-based algorithm was originally developed for MERIS and updated to become the C2RCC processor (Brockmann et al., 2016), which can also be locally applied by the users on Level-1 images. For instance, C2RCC was locally applied in this study (Section 2.3.2) to obtain OCNN-derived Rrs data, which are not written in the operational Level-2-products. In addition, there are small differences in the pre-processing steps between C2RCC applied by EUMETSAT ground segment and the locally processed C2RCC (further details in session 2.3.2), which also motivated the comparison here between L2-OCNN and locally applied C2RCC. Furthermore, the ESA ground segment approach uses a climatology of temperature and salinity for each pixel during processing, while locally processed C2RCC uses a constant value for the satellite scene (Brockmann Consult, personal communication). The L2-OCNN quality flags applied for the match-up analysis were: ‘Land’ and ‘Cloud’ (including cloud ambiguous and margin), ‘Invalid’, ‘Snow Ice’, ‘Cosmetic’, ‘Suspect’, ‘High solar zenith’, ‘Saturated’ and ‘OCNN_fail’ (EUMETSAT, 2018). The Level-2 ‘Highglint’ flag (raised when the sun glint correction is not reliable) showed no impact in the spectral performances, and the samples were kept (see discussion).

2.3.2. Case 2 Regional / Coast Colour processor (C2RCC) - locally processed

C2RCC processor was locally applied on Level-1 images through the software SNAP (v 6.0 – GPT tool) to derive Rrs , TSM, Chl-a and ADG443 through the NN inversion technique described in the previous session. C2RCC also computes absorption by CDOM at 443 nm by isolating this component from the absorption by detritus through the use of different spectral slopes (Brockmann et al., 2016). The differences between C2RCC applied by the ESA ground segment and the local processing through SNAP are related to pre-processing steps, such as (i) the “smile correction”, which consists of an instrumental correction of Top-of-Atmosphere (TOA) reflectance for small-scale variation of the channel's central wavelength in the image field-of-view, and (ii) the TOA reflectance correction for gaseous absorption. As part of the ground segment processing, these steps are applied before the system vicarious calibration (SVC) adjustments (EUMETSAT, 2018), while during local C2RCC processing (i.e., in SNAP), the SVC gains are applied directly to the Level 1B input products, i.e., the “smile correction” is not applied and the gaseous correction is applied within the NN. The impact of processing the data without smile correction in C2RCC is not quantified for OLCI, and methods for this correction in SNAP application are under discussion by the Sentinel-3 Validation Team. The SVC consists of

adjusting the top-of-atmosphere radiometry to meet the water-leaving radiance (L_w) requirements (i.e., L_w within 5% uncertainties), and it is applied after the instrumental radiometric calibration (i.e., pre-launch as well as post-launch on-orbit). The adjustment is performed through the indirect use of high-quality field data, generally L_w , concurrent with space acquisitions, in which dedicated gains (and possibly offsets) are generated to “force” the AC to reproduce these measurements. The gains are subsequently applied for the adjustment of TOA data (EUMETSAT, 2017). In this study, the same SVC gains used by ESA ground segment for the standard atmospheric processing were applied for the local processing of C2RCC, as recommended by the developers, although dedicated gains would be optimal.

There are two versions of C2RCC available to be locally applied: the standard version (C2RCC v1), which uses the same neural net as the L2-OCNN processing for complex waters, and the alternative version (C2RCC altNN), which is based on a revised simulation dataset applied to the ocean-atmosphere coupled model, including a larger number of samples and extended NN training ranges to cope with larger dynamic range for high backscatter waters such as rivers, estuaries and lakes (Brockmann Consult, personal communication). Note that the NN-based processors do not correct the data for BRDF effects. The C2RCC flags applied for the match-up analyses were: ‘Land’, ‘Coastline’, ‘Bright’, ‘Straylight risk’, ‘Invalid’, ‘Cosmetic’, ‘Saturated’, ‘Dubious’, ‘Cloud risk’ and ‘Out-of-Range’ (Rhow_OOR, Rtosa_OOR, Iop_OOR) (EUMETSAT, 2018). The C2RCC ‘Sunglint risk’ flag, estimated from the wind speed and Solar Zenith and Viewing Angles and inherited from Level-1B, was investigated and showed no interference in the radiometric match-ups, as explained in the previous section. The C2RCC ‘Out-of-Scope’ (Rtosa_OOS and Rhow_OOS) flags were investigated and showed no degradation of the data, with good quality Rrs spectra for both C2RCC versions. The ‘OOS’ flags depend on the threshold set by the user, and the default values may not be fully suitable for this area of interest, thus indicating that further analysis is needed to establish regional values (further details about flagging in the discussion).

2.3.3. POLYMER (POLYnomial based algorithm applied to MERIS)

POLYMER was originally developed to process MERIS data and has been extended to multiple sensors, such as MODIS, SeaWiFS, VIIRS and OLCI. Here, Level-1 data were processed using POLYMER v. 4.9. The processor uses two models to describe the spectral reflectance of the atmosphere and residual sun glint, using a polynomial formulation with respect to the wavelength, and the water reflectance, based on chlorophyll concentration and a coefficient (fb) that scales the backscattering coefficient of particles, bbp (Park and Ruddick, 2005). The analytical water reflectance model is valid for both case 1 and case 2 waters, including bidirectional effects. The algorithm scheme consists of using a spectral matching technique to optimize three parameters of the atmospheric model, which are coefficients of a polynomial formulation, and two parameters of the water reflectance model (Chl-a and bbp) using at least 5 bands in order to obtain the best spectral fit for the total reflectance measured by the sensor (Steinmetz et al., 2011; Steinmetz et al., 2016). TSM is computed by POLYMER through the linear relationship: $TSM = 100 * bbp650$ (from Neukermans et al., 2012, who defined $\log_{10}(bbp) = 1.03 * \log_{10}(SPM) - 2.06$). Here, Chl-a and TSM were considered direct outputs of POLYMER algorithm once Chl-a and bbp are derived as part of the optimization scheme, and applying a bio-optical algorithm to the water reflectance provided by POLYMER may lead to different results. The following flags were applied: ‘Cloud’, ‘Invalid’, ‘Negative BB’, ‘Out-of-bounds’, ‘Exception’, ‘High Air Mass’ and ‘Thick Aerosol’ (Steinmetz et al., 2016). As recommended by the documentation, the ‘Inconsistency’ and ‘Case-2’ flags should not invalidate the results, however, the match-up analysis suggested that the ‘Case-2’ flag could be used to improve the POLYMER-derived Chl-a L3 products (see Section 4.3 for the details).

2.4. Statistical analysis for algorithms validation

The performance of the different processors was evaluated through one-to-one match-up analyses of concurrent satellite data and *in situ* measurements. Match-up satellite data were obtained from a 3×3 pixel window centered in the *in situ* sampling location, with a maximum ± 2 h time difference (except for Chl-a data for which the time window was ± 5 h). The mean, median and coefficient of variation (CV) were computed for the different products of interest, provided a minimum of 5 pixels were available and $CV < 25\%$ (adapted from Bailey and Werdell, 2006). Selecting a more rigorous CV criterium would be ideal, however, it would lead to a limited number of match-ups that might no longer offer a suitable statistical basis for meaningful diagnostics (IOCGG, 2019). To minimize the impact of mismatch due to the time difference between sampling and satellite extracted data in such a dynamic region, the location of samples collected close to the Fraser plume was adjusted based on the dominant surface current direction as derived from a local CODAR system (Coastal Ocean Dynamics Applications Radar) (Halverson and Pawlowicz, 2016). The tidal currents in the SoG have a southeast-northwest orientation along the main axis of the strait due to the inflow of shelf waters through the southern entrance. Only four points were re-located for the satellite data extraction since most of the samples were obtained close to the time of slack water, a period with no strong tidal currents.

In order to compare the performance of the different algorithms in retrieving Rrs, the following statistical parameters have been used: the correlation coefficient (r), the mean BIAS ($BIAS_{Rrs}$, expressed in %) and the Median Absolute Percent Difference (MdAD; %), being defined as:

$$BIAS_{Rrs} = 100 \cdot \frac{1}{n} \sum_{i=1}^n \frac{|Sat_i - InSitu_i|}{InSitu_i} \quad (2)$$

$$MdAD = 100 \cdot \text{Median} \left| \frac{Sat_i - InSitu_i}{InSitu_i} \right| \quad (3)$$

where Sat_i is the satellite-derived data, $InSitu_i$ is the *in situ* measurement, and n is the number of samples. Unlike Rrs, statistical parameters for the biogeochemical products (BP: Chl-a, TSM and CDOM) were computed following a log-normal hypothesis. They are $BIAS_{BP}$ (Eq. 4), MdAD (Median Absolute Difference, Eq. (5)) and the parameters of a linear regression fitting (r and slope).

$$BIAS_{BP} = 10^r \left(\frac{\sum_{i=1}^n \log_{10}(Sat_i) - \log_{10}(InSitu_i)}{n} \right) \quad (4)$$

$$MdAD = 10^r \text{Median} |\log_{10}(Sat_i) - \log_{10}(InSitu_i)| \quad (5)$$

As $BIAS_{BP}$ was computed in the multiplicative space, it is dimensionless and the back-transformation from \log_{10} results in values closest to unity (i.e. $BIAS_{BP} = 1.0$) being the least biased, with $BIAS_{BP} > 1.0$ and < 1.0 representing over and underestimation, respectively (Seegers et al., 2018). For example, $BIAS_{BP} = 1.2$ represents a model overestimation of 1.2 times higher, or 20%, while $BIAS_{BP} = 0.8$ represents underestimation of -20% . MdAD is always above unity, and $MdAD = 1.5$ represents, for example, a median percent difference of 50%.

The overall performance of the algorithms in retrieving Chl-a, TSM and CDOM was analyzed by means of spider plots (Matlab package v2.2.1- https://github.com/NewGuy012/spider_plot), an effective graphical approach for evaluating the behaviour of algorithms across multiple statistical parameters after appropriate scaling and normalization (see details in Seegers et al., 2018 and references therein). Here, the spider plots center is the reference for better performance, such that the smallest polygon shape defines the best overall algorithm’s performance. The statistical metrics used in the spider plots were $BIAS_{BP}$, MdAD, n (number of valid samples) and the linear correlation parameters (r and slope). When performances were similar, the range of retrieved values was considered important, and higher priority was

given to difference metrics (BIAS_{BP} and MdAD) than to linear regression parameters.

2.5. OLCI Level-3 composites of Chl-a, TSM and CDOM for BC and SEA coastal waters

A batch of approximately 250 scenes from OLCI Sentinel-3A was processed through POLYMER (for Chl-a and TSM) and C2RCC altNN (for CDOM). POLYMER was processed through Python while C2RCC altNN was processed in SNAP (6.0) in batch mode using the GPT (Graphic Processing Tool). The dataset was selected based on valid pixel coverage, with only days with $> 60\%$ valid data across the entire area (cloud-free coverage) being used. Thus, the dataset included 15 to 20

daily mosaiced images of the study area for each season (Spring, Summer and Fall) from 2016 to 2018, from which seasonal trends were composed. Although few images were used, the seasonal composites presented excellent coverage and data quality for trend analyses that were based on averages and standard deviations. Level-3 binned composites were generated using GPT from SNAP. The same quality flags used in the Level-2 match-up analysis were applied for the Level-3 products (Section 2.3); however, based on the Chl-a validation results, the ‘Case-2’ flag from POLYMER was applied to the final Chl-a Level-3 composites to improve the estimates (section 3.1.4). Ultimately, satellite data from two latitudinal transects were extracted from the seasonal composites: a nearshore transect (about 2 to 10 km from the coast, depending on the region) and one over the external margin of the

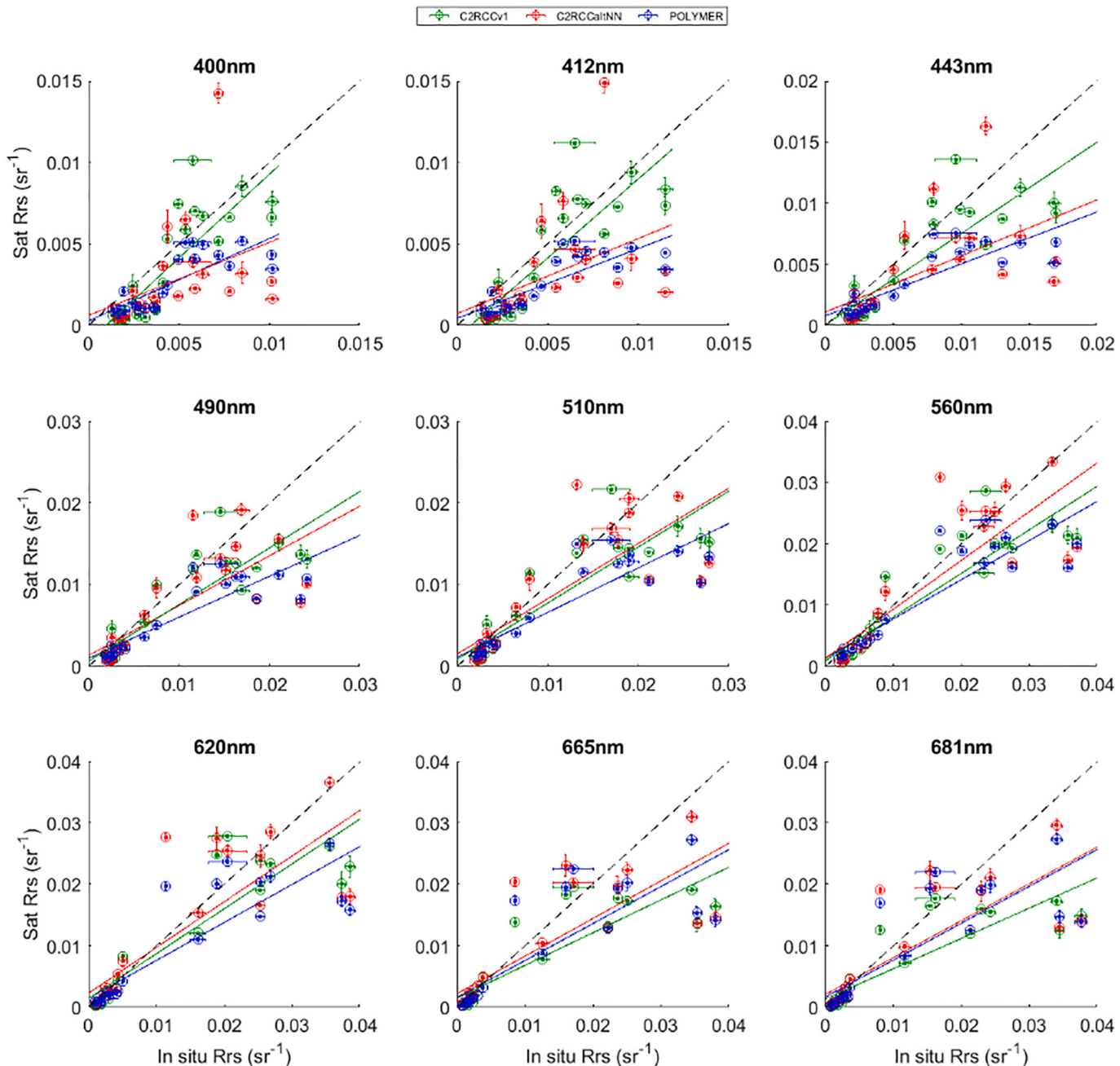


Fig. 2. Scatter plots of *in situ* Rrs versus satellite-derived Rrs for visible wavelengths. The dashed line is the 1:1 line, and coloured lines are linear regression fits for each processor (C2RCCv1 - green, C2RCC altNN – red, and POLYMER - blue). Error bars are ± 1 standard deviation within the satellite 3×3 pixels window and respective *in situ* measurements (corresponding radiometric data binning). (For interpretation of the references to colour in this figure legend, the reader is referred to the web version of this article.)

continental shelf (approximately over the 400 m isobath – see Fig. 1c). The transects data were averaged within a 6 km wide band, represented by a 21×21 pixels window in OLCI Sentinel-3A.

3. Results

3.1. Validation of OLCI Sentinel-3A products – match-up analysis

The Rrs match-up analysis showed that overall, the C2RCC v1 presented the best radiometric performance, while C2RCC altNN and POLYMER results were similar (Fig. 2). The major difference among processors was in the blue wavelengths, where C2RCC v1 showed the lowest BIAS_{Rrs} (around -32%), although the three approaches had large absolute differences (MdAD > 45%) (Table 1). For those bands, C2RCC altNN and POLYMER did not comprise the dynamic range of the *in situ* values, showing a certain degree of saturation for Rrs above 0.008 sr^{-1} (400 and 412 nm) and 0.012 sr^{-1} (443 nm) (Fig. 2). The results were similar for the green bands, and C2RCC altNN showed slightly better performance in the red bands with lower BIAS_{Rrs} and MdAD (Table 1).

The TSM match-ups showed similar results for L2-OCNN, C2RCC v1 and POLYMER, with the lowest BIAS_{BP} ($= 0.63$) found for POLYMER (Table 2). Although the C2RCC altNN had the best fitting slope, it had the largest match-up differences (BIAS_{BP} = 5.99 and MdAD = 5.69; Table 2), showing a significant overestimation of TSM. To a lesser extent, L2-ESA and C2RCC v1 also overestimated TSM concentrations (BIAS_{BP} = 2.14 and 2.78, respectively; Table 2). The multi-metrics analysis showed that POLYMER provided the overall best performance in retrieving TSM (Fig. 3a), and thus the correlation between *in situ* and POLYMER-derived TSM is presented in Fig. 3b.

Unlike L2-OCNN products, C2RCC processors, both v1 and altNN, provide estimates of CDOM absorption at 443 nm as an individual component, in addition to the conventional product ADG443 (absorption by detritus + gelbstoff at 443 nm). The two versions of C2RCC performed similarly in retrieving CDOM absorption (Fig. 4a; Table 3), however, C2RCC v1 did not capture the range of variability of the *in situ* measurements (Fig. 4b), which was considered an important metric. The maximum CDOM value estimated by the C2RCC v1 was 0.8 m^{-1} , while measured *in situ* CDOM data ranged from 0.2 to 5.0 m^{-1} . The C2RCC altNN provided an improved range (0.04 to 10.0 m^{-1}) as expected due to the extended neural nets range. However, the overall performance of C2RCC altNN to retrieve CDOM was still poor (MdAD = 3.85 and slope = 1.50), with a significantly fewer number of valid samples ($N = 31$; Table 3).

Given the differences found (MdAD > 3.00 and BIAS_{BP} around 0.30; Table 3) in retrievals of CDOM from C2RCC (v1 and altNN), we also evaluated the ADG443 retrievals against *in situ* CDOM data. The results showed an overall improvement, with BIAS_{BP} closest to 1.00 and MdAD < 1.60 (Table 3). L2-OCNN and C2RCC v1 exhibited similar results, as expected. However, despite the better linear fitting parameters compared to the C2RCC altNN (Fig. 4a), both versions did not retrieve the dynamic range of *in situ* values (Fig. 4b). Furthermore, slope and r from C2RCC altNN were driven by one outlier sample (Fig. 4c). Thus,

Table 2

Validation of OLCI Sentinel-3A retrievals of TSM (mg/L). Statistical parameters were obtained from the log-transformed data.

	L2- OCNN	C2RCC v1	C2RCC altNN	POLYMER
n	31	27	30	32
r	0.93	0.94	0.80	0.92
Slope	1.33	1.36	1.01	1.18
BIAS _{BP}	2.14	2.78	5.99	0.63
MdAD	2.18	2.44	5.69	2.03

ADG443 from C2RCC altNN was considered the best proxy for *in situ* CDOM distribution (Fig. 4d).

The correlations between *in situ* and satellite-derived Chl-a were generally weak (r and slope < 0.40; Table 4). L2-OCNN provided similar relative (BIAS_{BP}) and absolute (MdAD) differences to the locally processed C2RCC v1 (Fig. 5a), but showed opposite trends, slightly underestimating Chl-a (BIAS_{BP} < 1.0; Table 4). These approaches yielded the largest absolute differences with MdAD > 2.70, representing a difference of 170%. Among the four approaches, C2RCC altNN had the largest BIAS_{BP} (Table 4). This processor, however, showed better performance than C2RCC v1, being closer to the POLYMER multi-metric response (Fig. 5a). POLYMER retrieved the largest number of valid data points ($n = 95$) and showed slightly better overall performance than C2RCC altNN (Fig. 5a), and as such was considered the best approach. The relationship between *in situ* and POLYMER-derived Chl-a is presented in Fig. 5b.

Further analysis showed that the samples in which the POLYMER ‘Case-2’ flag was raised had the largest deviations from *in situ* Chl-a (gray points in Fig. 5b). By removing those samples (named ‘Case-2’ samples hereafter), POLYMER retrievals yielded a noticeable improvement in statistical performance, with BIAS_{BP} closest to 1.0 (0.99) and MdAD = 1.82, which represents a median difference of about 82%. POLYMER still provided a larger number of valid data points ($n = 83$) than NN-based models after the ‘Case-2’ samples were flagged out. Notably, an underestimation of high Chl-a levels was observed for POLYMER retrievals (Fig. 5b), likely influencing the slope of this correlation, which increased to 0.53 (slope) after removing the outlier sample (*in situ* Chl-a = 120 mg.m^{-3}). Nonetheless, the overall statistical performance of POLYMER was not improved when this sample was removed from the analysis.

We further investigated the radiometric performance of POLYMER by dividing the Rrs match-up samples into ‘non Case-2’ and ‘Case-2’ (Section 3.1) and computing the validation statistics for each group (Fig. 6). For comparison, C2RCC v1 and altNN-derived Rrs are also shown. The relative BIAS for POLYMER did not differ between the two groups, and, in fact, the C2RCC retrievals showed smaller BIAS than POLYMER for the turbid “Case-2” samples (Fig. 6b). Similarly, the absolute differences were not expressively different between the two groups for POLYMER (MdAD between 25 and 55%, with larger differences in the blue bands for both groups), and the C2RCC versions showed even larger differences for the ‘non-Case-2’ samples (Fig. 6a), suggesting slightly worse performance in clearer waters. The coefficients

Table 1

Statistical match-up results for OLCI Sentinel-3A Rrs against *in situ* Rrs ($n=24$) for the different processors (C2RCC v1, C2RCC altNN and POLYMER).

λ	C2RCC v1			C2RCC altNN			POLYMER		
	r	BIAS _{Rrs}	MdAPD	r	BIAS _{Rrs}	MdAPD	r	BIAS _{Rrs}	MdAPD
400 nm	0.83	-33.1	52.83	0.41	-43.2	61.58	0.80	-43.3	47.79
412 nm	0.84	-31.5	50.08	0.46	-40.5	57.43	0.82	-47.2	54.32
443 nm	0.86	-33.6	44.98	0.60	-36.9	47.24	0.85	-41.5	49.71
490 nm	0.88	-28.7	42.12	0.77	-25.9	36.30	0.88	-35.3	39.94
510 nm	0.89	-27.5	42.02	0.80	-20.5	28.86	0.89	-31.2	35.05
560 nm	0.91	-28.8	38.85	0.85	-18.2	31.54	0.91	-23.6	31.09
620 nm	0.89	-25.3	39.77	0.83	-7.2	30.73	0.87	-26.8	34.65
665 nm	0.87	-36.3	43.11	0.81	-12.0	30.69	0.84	-28.4	37.47
681 nm	0.86	-42.7	51.25	0.80	-18.1	39.37	0.83	-26.4	36.31

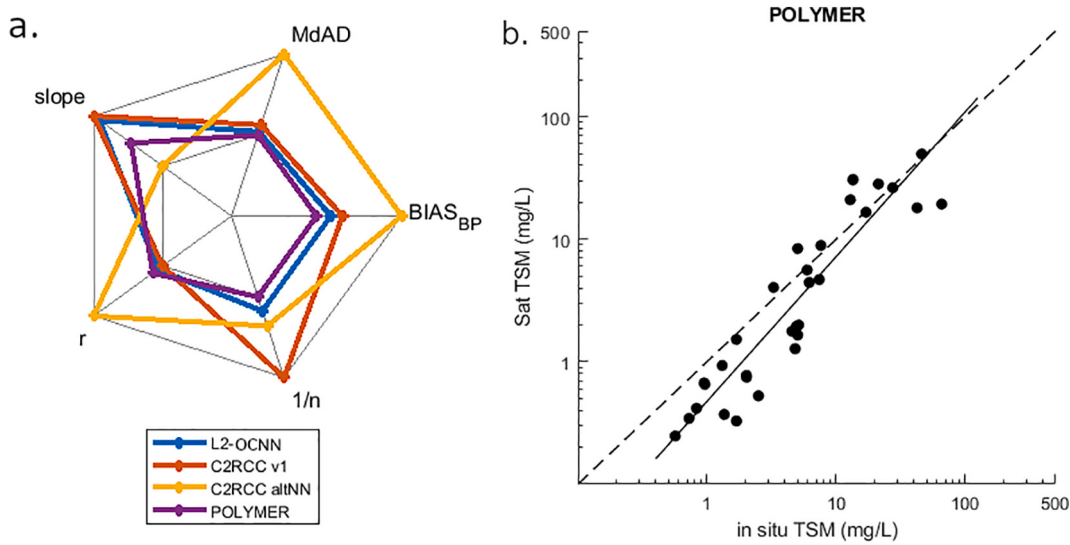


Fig. 3. (a) Spider plot for TSM algorithms validation based on the multi-metrics approach and (b) the linear correlation between *in situ* and POLYMER-derived TSM. The dashed line represents the 1:1 line.

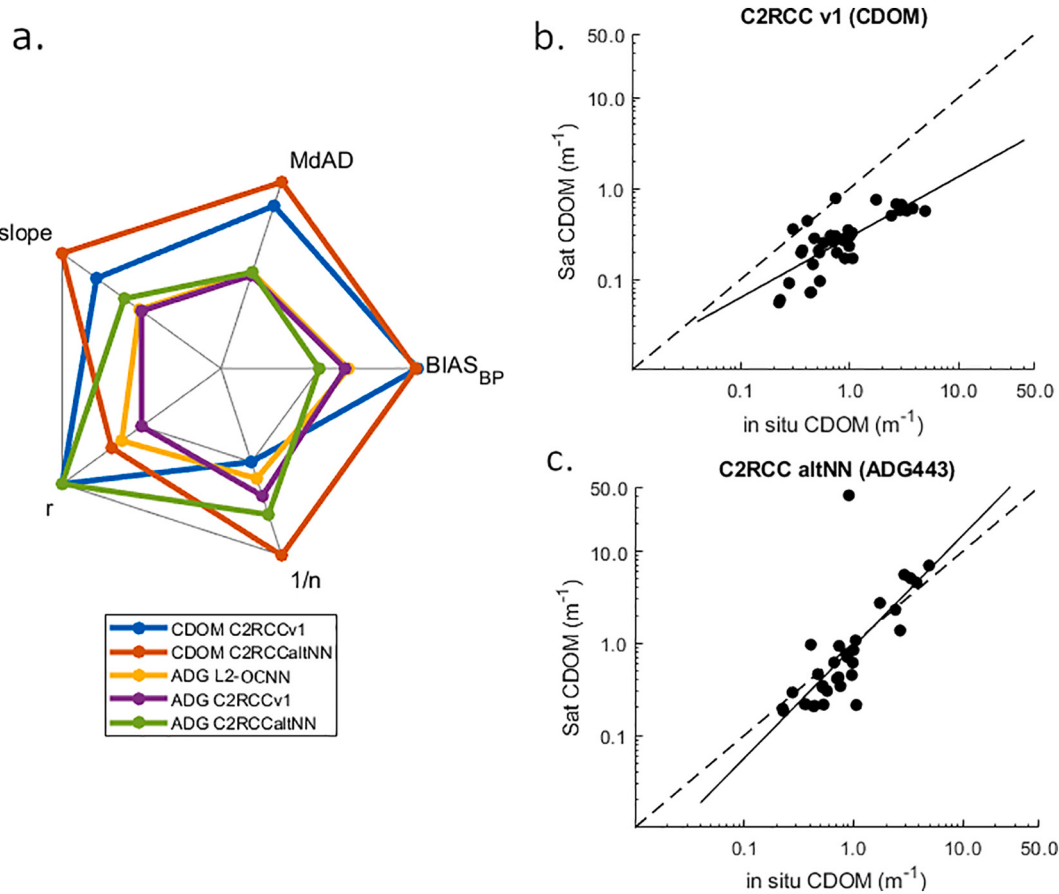


Fig. 4. (a) Spider plot for CDOM and ADG443 algorithms validation, based on the multi-metrics approach. (b) Linear correlation between *in situ* CDOM absorption and CDOM absorption derived from C2RCC v1. (c) Linear correlation between *in situ* CDOM absorption and ADG443 derived from C2RCC altNN.

of correlation for the ‘Case-2’ samples were weak for the three models ($r < 0.7$), and clearly showed that samples tagged as ‘Case-2’ by POLYMER had highly scattered linear fit and saturation of Rrs retrieved by the algorithms in those turbid waters (Fig. 6b).

3.2. OLCI Sentinel-3A retrievals for British Columbia and Southeast Alaska: seasonal trends

The trends for Spring, Summer and Fall in BC and SEA were obtained from latitudinal transects of POLYMER-derived TSM and Chl-a, and C2RCC-derived ADG443 (referred to as CDOM hereafter) on the

Table 3

Validation of OLCI Sentinel-3A retrievals of absorption by CDOM (m^{-1}) and the combined product ADG (Detritus + CDOM; m^{-1}). Statistical parameters were obtained from the log-transformed data.

	CDOM (gelbstoff)		ADG443		
	C2RCC v1	C2RCC altNN	L2-OCNN	C2RCC v1	C2RCC altNN
n	36	31	35	34	33
r	0.75	0.80	0.81	0.83	0.75
Slope	0.66	1.50	1.14	1.13	1.21
BIAS _{BP}	0.31	0.32	0.71	0.73	0.88
MdAD	3.25	3.85	1.56	1.49	1.57

Table 4

Validation of OLCI Sentinel-3A retrievals of Chl-a (mg.m^{-3}). Statistical parameters were obtained from the log-transformed data.

	L2-OCNN	C2RCC v1	C2RCC altNN	POLYMER	POLYMER 'Case-2' flagged out
n	53	63	74	95	83
r	0.35	0.13	0.16	0.18	0.51
Slope	0.35	0.15	0.08	0.14	0.30
BIAS _{BP}	0.74	1.31	1.42	1.36	0.99
MdAD	2.73	2.93	2.24	2.13	1.82

nearshore and continental shelf (dashed lines in Figs. 7a, 9a and 11a); these were the best performance retrievals (Section 3.1). The three products showed values within the range observed in the *in situ* dataset used in this study.

Fig. 7 shows the distribution of TSM in each season, with overall larger values during the Summer (Fig. 7b). TSM varied on average from 0.2 to 25.0 mg/L along the nearshore transect and 0.1 to 1.5 mg/L along the shelf transect (Fig. 8). In BC, the highest concentrations were observed in Spring-nearshore and Summer-nearshore for the Fraser River's plume waters (up to 23.4 ± 16.6 mg/L). Nearshore waters around 54°N, which were likely influenced by the Skeena and Nass rivers, also exhibited high TSM in both Spring and Summer (up to 11.1 ± 7.1 mg/L) (Fig. 8a, b). In SEA, the most significant TSM contributions were in nearshore waters in the vicinity of the Stikine River (56°N) all year round and the Alsek River (59°N) in Spring and Summer (see rivers location in Fig. 7a). Different dynamics were observed in the TSM distribution for BC and SEA nearshore waters: the BC coast showed larger TSM peaks in Spring, while the SEA showed higher TSM in Summer and

Fall (Fig. 8b, c). This difference was coupled with the dynamics of the riverine discharges, with the largest volume of water discharged in BC in late Spring, while in SEA, the largest volumes were observed in mid and late Summer (Fig. 9). Along the continental shelf, the largest TSM concentrations (maximum of 1.42 ± 0.75 mg/L) were observed during the Summer on the west coast of Vancouver Island (between 48.5 and 51°N; Fig. 8b).

ADG(443) was used as a proxy to map CDOM (Fig. 10) and, in general, the highest CDOM values were observed in the Strait of Georgia in Spring and Summer (Fig. 10a, b) and along the SEA coast in the Fall (Fig. 10c). In the SoG, CDOM mean values reached up to $4.4 \pm 6.1 \text{ m}^{-1}$ (Fig. 11b), likely influenced by the Fraser River plume waters. Unlike the TSM, CDOM levels were lower in the SoG compared to northern waters in the Fall (Fig. 11c). High CDOM loads were observed close to the mouth of the Skeena and Nass rivers in Spring ($1.1 \pm 0.9 \text{ m}^{-1}$, Fig. 11a), and in the coastal waters of east Hecate Strait (BC Northern Coast, around 53°N) during Summer and Fall, reaching values of $1.5 \pm 2.5 \text{ m}^{-1}$ and $1.9 \pm 2.8 \text{ m}^{-1}$, respectively (Fig. 11b, c). On the continental shelf, CDOM values were generally the lowest ($<0.5 \text{ m}^{-1}$), restricted to the west coast of Vancouver Island (49 to 51°N) in the Summer (Fig. 11b) and the outer shelf of the SEA (56 to 58°N) in the Fall (Fig. 11c).

Despite the caveats with satellite-derived Chl-a estimates in coastal waters, the overall seasonal and latitudinal values found for the entire study area were within expected ranges (Fig. 12). In the nearshore, mean Chl-a values varied from 1.8 ± 0.5 to $10.6 \pm 4.3 \text{ mg.m}^{-3}$, with maximum values in the central SoG in Spring (Fig. 13a) and the vicinity of the Stikine River mouth (56.5°N) in the Summer (Fig. 13b). In contrast, the lowest Chl-a values were observed in Johnstone Strait (51°N, coastal transect) and northern SEA waters, except by the Alsek river mouth (Fig. 13). On the central and northern BC coast, Chl-a ranged from 2.0 ± 0.6 to $6.0 \pm 4.0 \text{ mg.m}^{-3}$ in Spring and Summer, respectively. High Chl-a values were observed near Calvert Island (51.5°N, coastal transect) in the Fall (up to $5.0 \pm 1.7 \text{ mg.m}^{-3}$; Fig. 13c). On the continental shelf, relatively high Chl-a concentrations were observed on the west coast of Vancouver Island in Spring and Summer (ranging from 1.4 ± 0.6 to $4.8 \pm 1.8 \text{ mg.m}^{-3}$; Fig. 13a, b), with large variability expressed by the high standard deviations. The SEA shelf was relatively productive from Spring to Fall, with values ranging from 0.63 ± 0.18 to $2.70 \pm 2.9 \text{ mg.m}^{-3}$, while BC central shelf region, between Haida Gwaii and Vancouver Island (see Fig. 1c) was relative lower, overall, below 2.0 mg.m^{-3} .

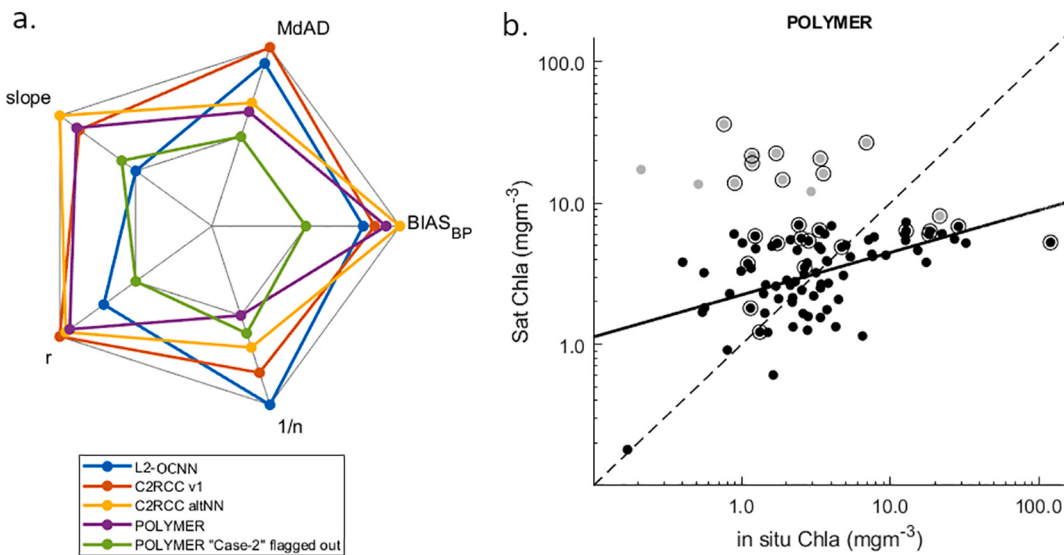


Fig. 5. (a) Spider plot for Chl-a validation, based on the multi-metrics approach and (b) the linear correlation between *in situ* and POLYMER-derived Chl-a. The fit line (solid black line) does not include samples flagged as 'Case-2' by POLYMER (gray points). Circled points indicate samples for which *in situ* Rrs were available.

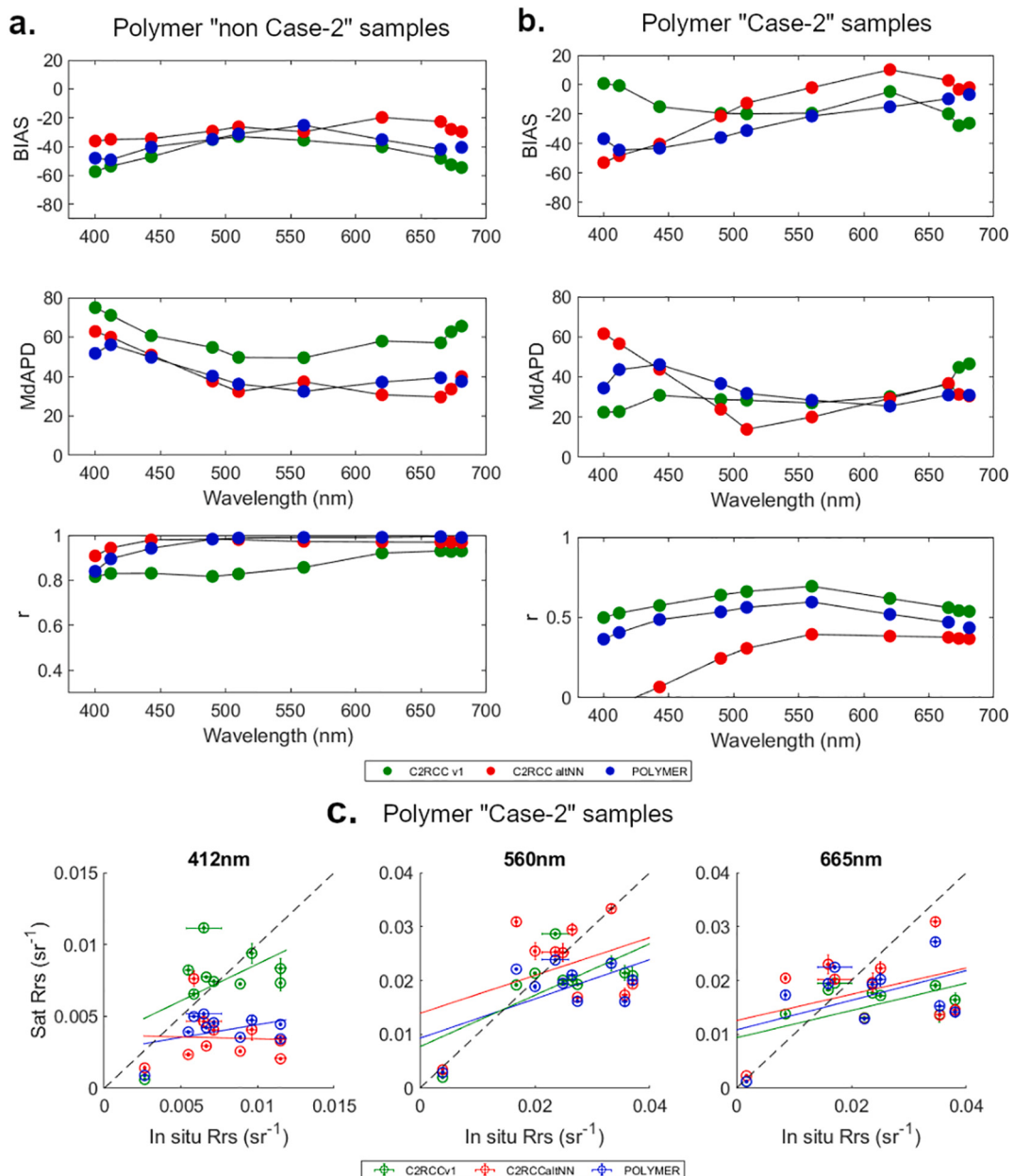


Fig. 6. Statistical metrics (BIAS_{Rrs} , MdAPD and r) for Rrs match-ups for two groups derived from Chl-a match-ups: (a) samples for which the POLYMER ‘Case-2’ flag was not raised and (b) samples for which the ‘Case-2’ flag was raised. Note that C2RCC match-ups corresponding to the same samples are also presented. (c) Scatter plots of *in situ* Rrs versus satellite-derived Rrs at 412, 560 and 665 nm for samples in which the “Case-2” flag was raised when processed through POLYMER.

4. Discussion

4.1. Performance of OLCI Sentinel-3A processors for coastal waters based on match-up samples

Despite previous work on accuracy assessment of MODIS-Aqua retrievals in a limited area of British Columbia (Carswell et al., 2017; Hilborn and Costa, 2018), this study comprises the first attempt to retrieve data from OLCI Sentinel-3A over the entire BC and SEA coastal waters, while evaluating the performance of different processors for retrieval of biogeochemical products, allowing the use of validated satellite products for better understanding the dynamics of these complex waters. The southern coastal waters of British Columbia are characterized by a high optical complexity (Komick et al., 2009; Loos and Costa, 2010; Carswell et al., 2017; Loos et al., 2017; Phillips and Costa, 2017). Although those studies were restricted to southern BC, a similar

level of complexity is expected in the central and northern BC and Southeast Alaska, given the similar complex nearshore geomorphology, characterized by the presence of straits, sounds, inlets and fjords, and the large volume of freshwater and associated terrestrial material discharge (Thomson, 1981; O’Neel et al., 2015). The optical complexity of the region prevents accurate retrievals from ocean colour imagery processed with standard AC techniques (Carswell et al., 2017). However, approaches adapted for MODIS-Aqua using the Management Unit of the North Seas Mathematical Models (Ruddick et al., 2000), considering both the NIR and SWIR bands for the atmospheric correction and the OC3M for Chl-a estimation, have shown lower deviations when retrieving surface Rrs and Chl-a (Carswell et al., 2017). In this study, we evaluated other approaches applied to OLCI images to calculate bottom of atmosphere reflectances and biogeochemical products, such as C2RCC, which uses an artificial neural network, and POLYMER, which uses spectral optimization, both based on a coupled model for ocean-

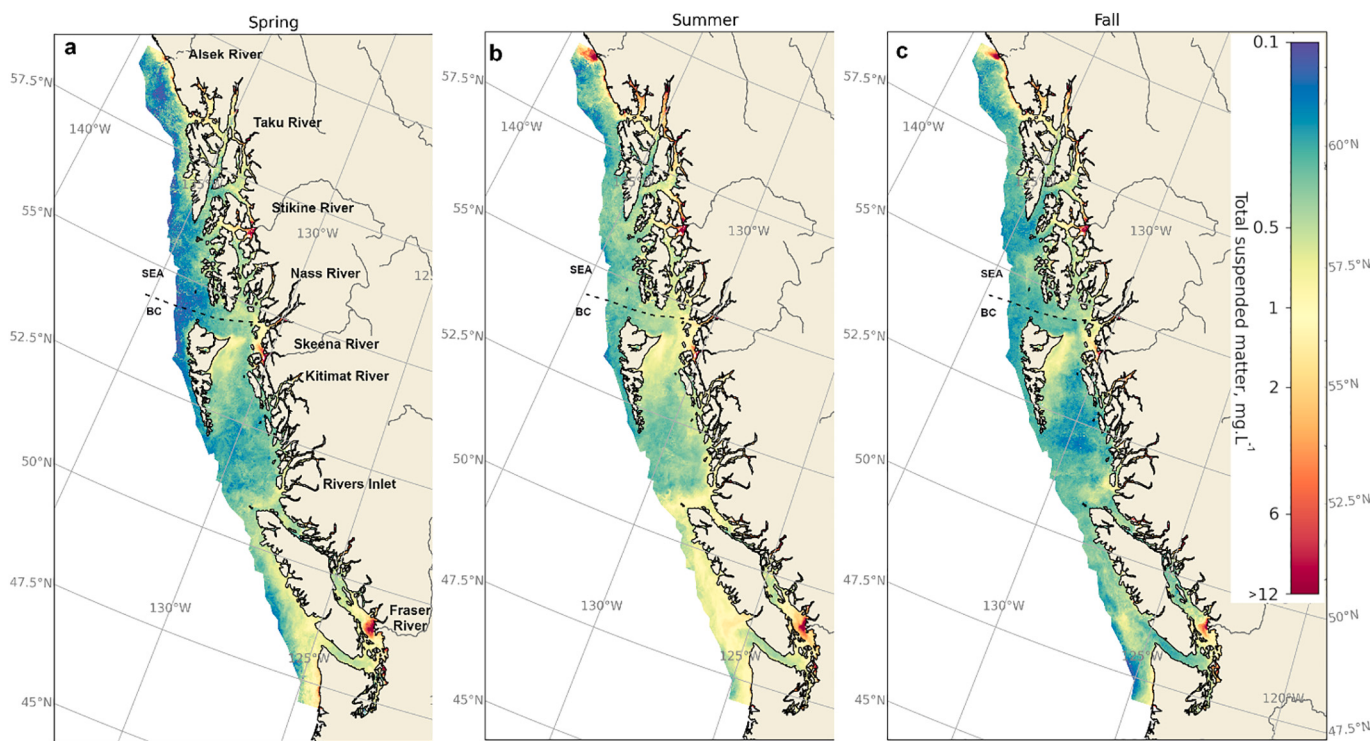


Fig. 7. OLCI-derived TSM maps from POLYMER (v 4.9) for (a) Spring, (b) Summer and (c) Fall along British Columbia and Southeast Alaska. Major rivers discharging to the coastal waters are identified in (a).

atmosphere. These approaches estimate bio-optical and biophysical products using the sensor's spectral resolution, *i.e.*, the more bands, the more refined the fit of the model, rather than the two-band Rrs ratio techniques, such as the OC3M and OC4 (O'Reilly et al., 2000).

Both C2RCC and POLYMER are currently under evaluation for OLCI Sentinel-3 applications, especially in coastal waters. For instance, several authors have shown improved performance for Sentinel-2 and Sentinel-3A retrievals compared with other processors such as ACOLITE, iCOR, NASA l2gen, Sen2Cor and ESA baseline atmospheric correction for distinct coastal and inland waters (Warren et al., 2019; Pereira-Sandoval et al., 2019; Mograne et al., 2019). Our match-up results showed percent differences between 23.6 and 50.5% for Rrs retrievals from C2RCC (v1 and altNN), except for the blue bands where the altNN reached 59.4% difference. Similar poor performance in the blue bands was also reported by Mograne et al. (2019) for Sentinel-3 with C2RCC processor. Overall, our results showed a slightly better performance of C2RCC v1. One possible explanation is that the altNN might be more impacted by the use of non-dedicated SVC gains, as the extended NN ranges may allow for a larger variability in water-leaving radiance spectra for regions highly impacted by the presence of CDOM and detritus, especially in the blue bands. However, a specific study should be performed to investigate whether this would be a causal effect.

Similar to C2RCC altNN, POLYMER showed relatively poor performance in the blue bands, which was also reported for MODIS when compared to the NASA standard AC (Zhang et al., 2018). The authors suggested that this is likely associated with POLYMER not adequately considering the CDOM contribution to the Chl-a signal in the reflectance modelling. POLYMER optimizes the reflectance signal above the water-air interface using initial values for Chl-a concentration and f_b , a coefficient that scales the backscattering coefficient of the particles (Steinmetz et al., 2016). As such, it does not consider a parameter directly related to non-covarying CDOM absorption at this processing step. Indeed, CDOM is one of the dominant optical constituents in our region (Loos and Costa, 2010; Phillips and Costa, 2017), and, here, we reported *in situ* CDOM ranging from 0.23 to 4.91 m⁻¹ (Fig. 3). Despite this

limitation, we showed that C2RCC and POLYMER tended to perform better in the OLCI blue bands than previously reported deviations obtained by the Level-2 baseline AC in CDOM-dominated waters (Zibordi et al., 2018). The authors found large percent differences for Lwn retrievals (up to 200% due to the low *in situ* values in the blue) due to the negative radiance values likely associated with overcorrection of atmospheric effects, which was not observed for C2RCC and POLYMER. Similarly, negative Rrs values derived from the operational Level-2 baseline AC were observed in our study (not shown), thus reinforcing the higher capability of the tested algorithms to better perform over CDOM-dominated waters. Although this analysis is based on match-up points covering a good dynamic range for this region, we acknowledge the limitation in the number of samples and the need for further radiometric validation with a larger dataset.

Although C2RCC v1 resulted in a better radiometric performance in the blue bands, the statistical evaluation of the biogeophysical products showed that overall POLYMER performed better at retrieving TSM and Chl-a than the NN approaches. As expected, the differences between the L2-OCNN and C2RCC v1 were relatively small, likely influenced by the different number of observations as the cloud masking and recommended flags are different, similar to observations by Kyryliuk and Kratzer (2019). The overall lower performance of C2RCC in relation to POLYMER may be associated with the default scaling factors used to convert IOP into TSM and Chl-a. The factors currently used to convert scattering at 443 nm into TSM ($TSM = 1.06 * b^{\text{tot}}^{1.72}$; where b^{tot} is the total scattering at 443 nm) is likely not appropriate for our waters, causing a large overestimation in TSM concentrations. Improvements on the C2RCC retrievals can be achieved when regional scaling factors are well established (*e.g.*, Kyryliuk and Kratzer, 2019), which depends on the nature of the particulate material for each area. In our region, bio-optical data are available only for the Strait of Georgia, where total particulate scattering was reported to vary from approximately 0.2 to 16.0 m⁻¹ in the blue spectral wavelengths (Loos and Costa, 2010; Phillips and Costa, 2017). The high scattering values are related to the high concentration of fine inorganic particles (Loos and Costa, 2010)

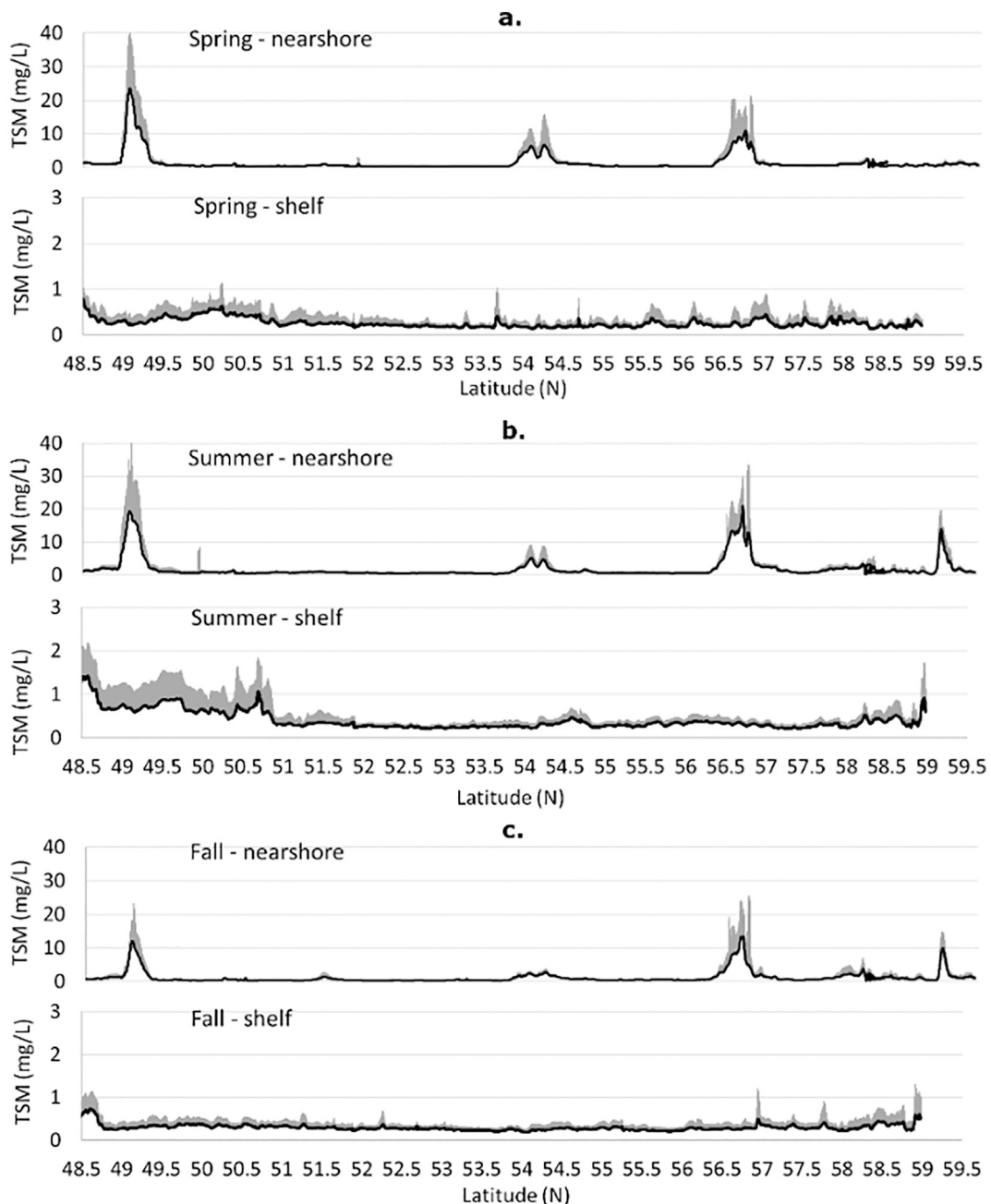


Fig. 8. Latitudinal distribution of TSM for (a) Spring, (b) Summer, and (c) Fall along nearshore and continental shelf transects in British Columbia and Southeast Alaska (Fig. 1c). TSM values are seasonal averages with the positive standard deviations indicated by the gray area. Note different y-axis scales for nearshore and continental shelf plots.

and are above the average of values observed for most open and coastal waters (Boss et al., 2013), but comparable to values observed in estuaries (e.g., Babin et al., 2003) and lakes (e.g., Lyu et al., 2015). Those reported scattering values are within the NN training dataset; however, establishing a broad relationship to convert the IOPs into bio-physical products is challenging when the objective is to map such a large and complex coastal margin, such as BC and SEA. This region-specific requirement was not observed for POLYMER, and likely the used relationship to compute TSM from particulate backscattering at 650 nm (Neukermans et al., 2012; Steinmetz et al., 2016) has a broader application. As such, POLYMER-derived TSM products exhibited high accuracy ($\text{BIAS}_{\text{BP}} = 0.63$ and $\text{MdAD} = 2.03$) compared to the other approaches. Furthermore, the model has the advantage of faster processing, being at least two times faster than C2RCC for the same

computational resource.

As discussed for TSM, the high deviations in Chl-a retrievals from C2RCC indicated that the scaling factor applied to estimate Chl-a from the phytoplankton pigment absorption at 443 nm ($\text{Chl-a} = a_{\text{pig443}} \hat{=} 1.04 * 21.0$) did not properly address such a relationship in our region. Our *in situ* vs C2RCC Chl-a data suggested that the exponent used by the model ($=1.04$) should be higher to minimize the overestimation observed in the low range of Chl-a values. Proposing a new exponent for this relationship would be too speculative without proper validation of a_{pig443} estimates. This relationship varies primarily according to the size structure of the phytoplankton population and the relative concentration of photosynthetic and accessory pigments (Giotti et al., 2002; Bricaud et al., 2004), which modulates the pigments self-shading within the cells, or package effect (Morel and Bricaud, 1981). Therefore, the scaling

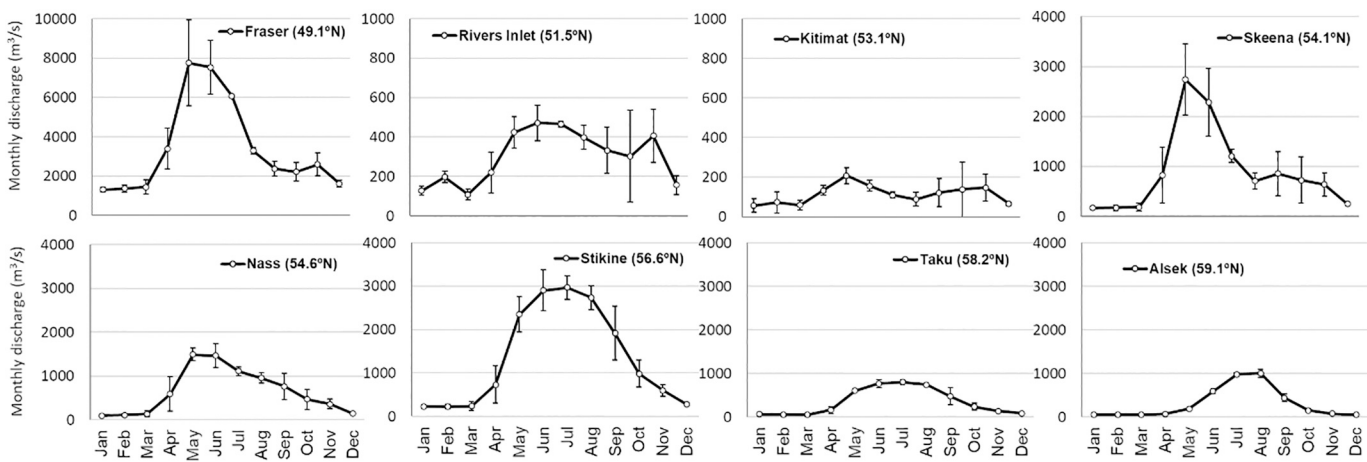


Fig. 9. Monthly freshwater discharge (mean \pm standard deviation) of the major rivers in British Columbia and Southeast Alaska from 2016 to 2018, obtained from Environment and Climate Change Canada (<https://wateroffice.ec.gc.ca/>). The indicated latitude is the approximate position of the river mouth to the sea. Note different y-axis scales.

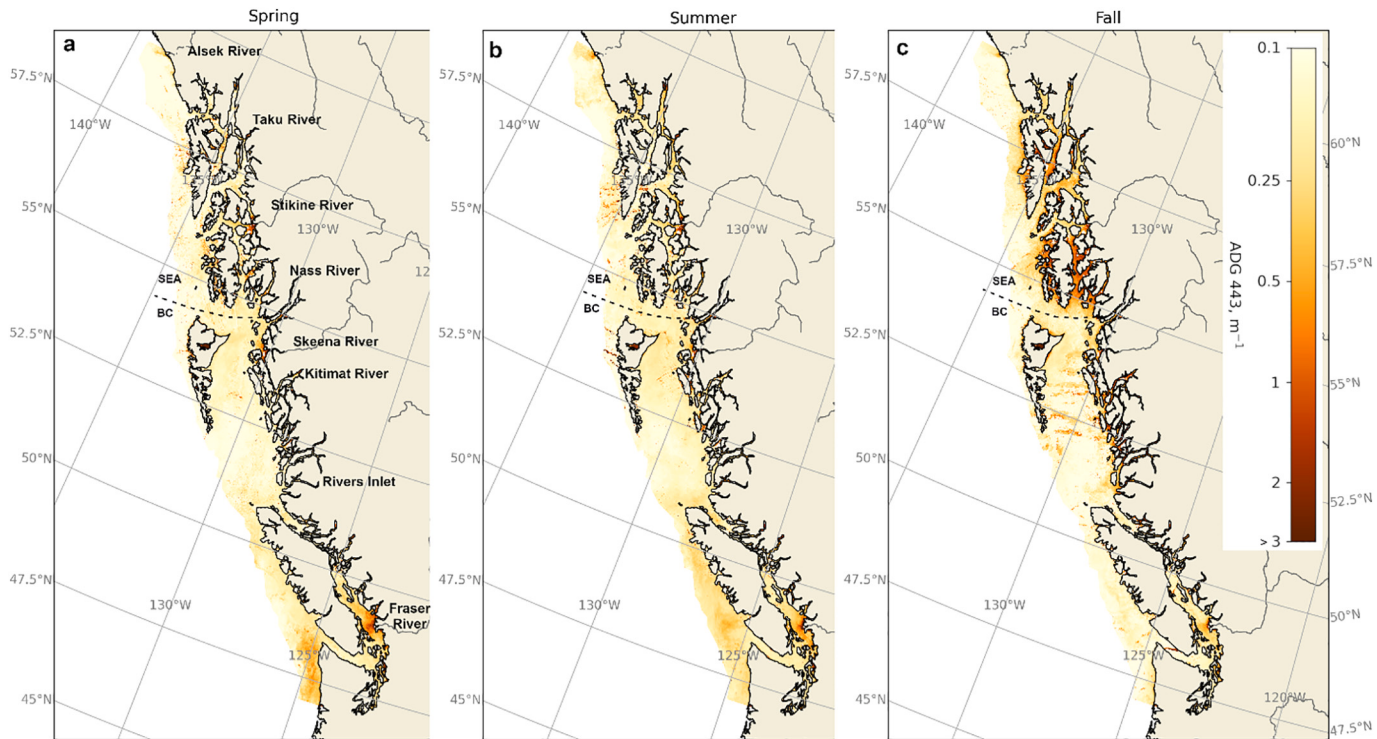


Fig. 10. OLCI-derived ADG(443) (CDOM proxy) maps from C2RCC altNN (or v2) for (a) Spring, (b) Summer and (c) Fall along British Columbia and Southeast Alaska.

factor used to define Chl-a is highly variable not only geographically and seasonally but also according to specific physiological and environmental conditions. Despite the scaling factor limitations, likely contributing to the poor performance of C2RCC in retrieving Chl-a relative to POLYMER, we believe that the output of Chl-a and TSM from POLYMER was further optimized by compensation for radiometric deviations through good preservation of the spectral shape in relation to the *in situ* data (Fig. 14). This will have a direct impact on the Chl-a estimation that is a by-product of the spectral matching procedure. The Chl-a retrievals significantly improved when the ‘Case-2’ flagged data were masked out. These flagged out data were associated with low *in situ* vs satellite radiometric correlation due to a large underestimation of high Rrs values (Fig. 6c). Such high Rrs values usually occurred as a

result of TSM loads in Spring and Summer, due to the discharge of fine inorganic particles from the Fraser River (Johannessen et al., 2006), resulting in highly scattering waters (Loos and Costa, 2010; Phillips and Costa, 2017). Similarly, Mograne et al. (2019) suggested that OLCI data processed by POLYMER may be affected by high values of turbidity where Chl-a is not the dominant optical component. Even though the Strait of Georgia is considered a dynamic Case-2 water body (Hilborn and Costa, 2018), POLYMER ‘Case-2’ flag only masked out the few pixels where the plume strongly affects the turbidity, and can still be used as a mandatory flag in coastal Case-2 waters without compromising data coverage. Further, it is important to highlight that the *in situ* Chl-a data were obtained from different protocols, and about 50% of our samples were analyzed using the fluorometric method (Chandler et al., 2018),

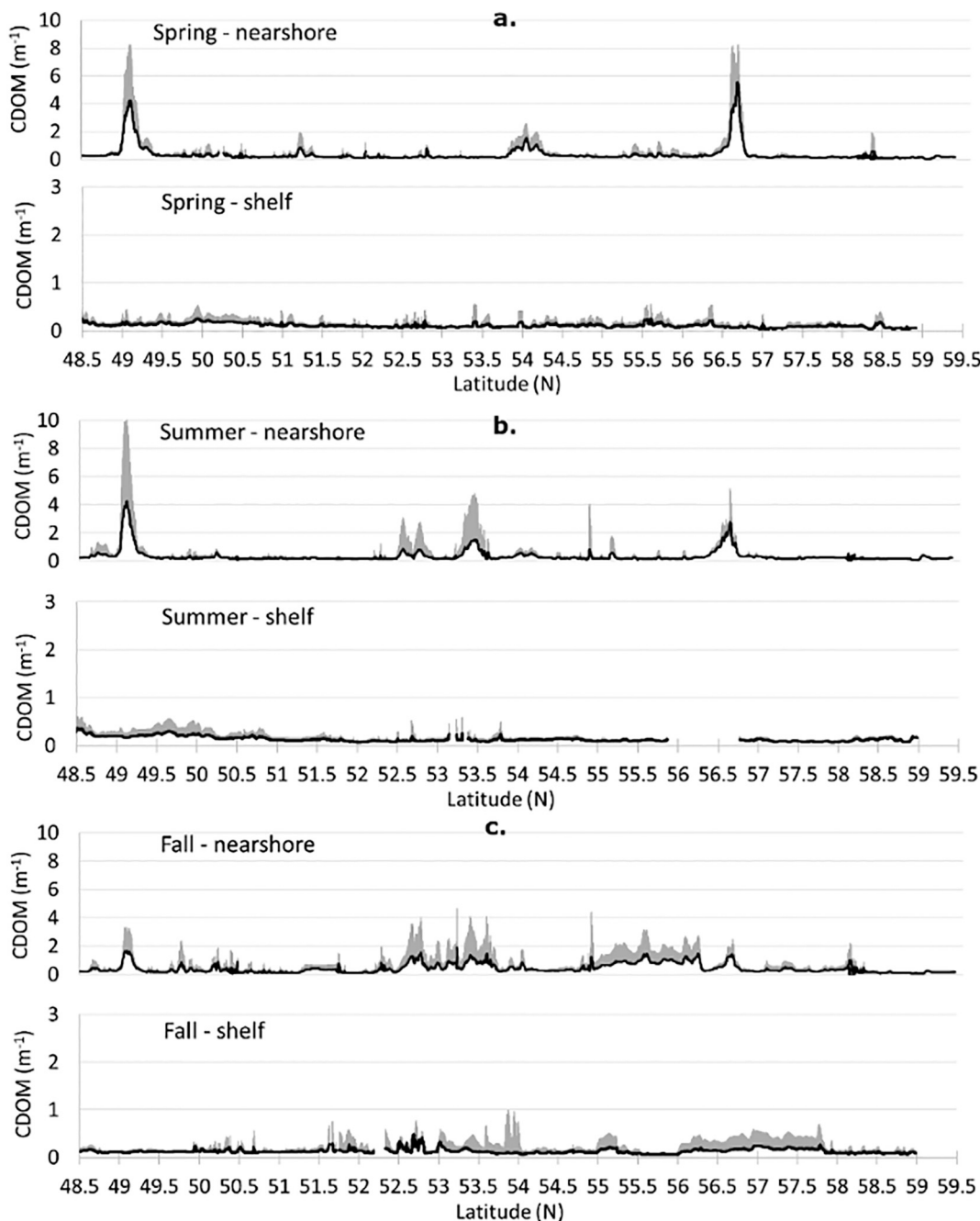


Fig. 11. ADG(443) (CDOM proxy) latitudinal distribution for (a) Spring, (b) Summer, and (c) Fall along nearshore and continental shelf transects in British Columbia and Southeast Alaska. ADG(443) values are seasonal averages with positive standard deviations indicated by the gray area. Note different y-axis scales for nearshore and continental shelf plots.

which has implications for the *in situ* Chl-a data uncertainties that we were not able to quantify.

The technical design of POLYMER to retrieve data under sun glint conditions and semi-transparent clouds leads to a gain of spatial coverage (Steinmetz et al., 2011). Thus, as a complementary analysis, we compared the results when coincident match-up data are used for both POLYMER and C2RCC altNN ($N = 73$), once the altNN showed better performance than v1. In this analysis, the C2RCC altNN slightly outperformed POLYMER, suggesting the overall better performance of POLYMER being associated with larger data coverage. However, when the POLYMER Case-2 flag was applied (reducing the match-up dataset to $N = 61$), significantly better results were still obtained for POLYMER, being close to the initial statistical differences. Thus, the advantages of

POLYMER retrievals can be summarized as larger data coverage, the presence of a flag that removes poor Chl-a estimates, the higher compatibility of the bio-optical relationships applied in the model for our study region (in comparison to C2RCC), and faster data processing. The development of these processors is a very dynamic field, and new versions of POLYMER with updated SVC gains will likely provide even more accurate retrievals in future applications. Finally, it is important to mention that Chl-a derived from the L2 BAC processing chain (OC4Me-derived Chl-a; Morel et al., 2007) performed the poorest in our coastal waters (not shown).

Unlike TSM and Chl-a, which are biophysical products and require a scaling factor to be computed from the IOPs, CDOM absorption and ADG443 are bio-optical products directly inverted by the C2RCC

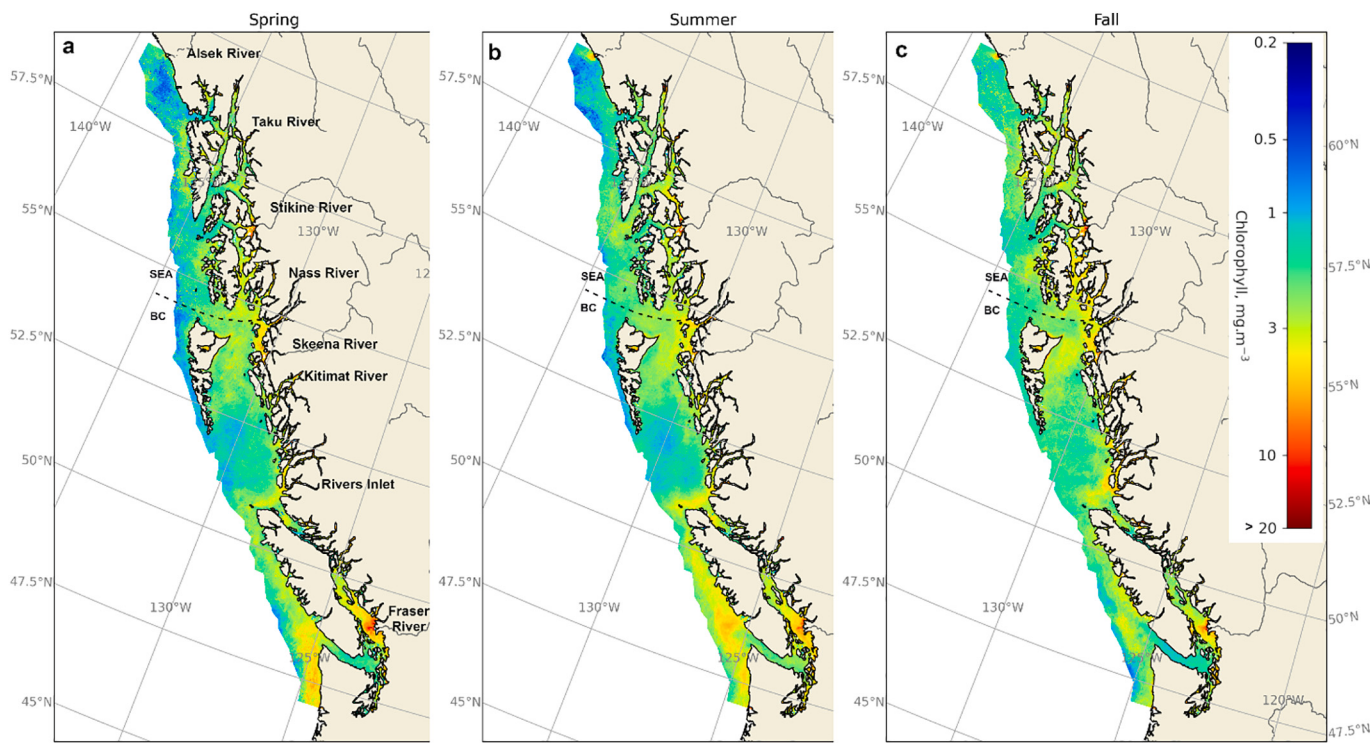


Fig. 12. OLCI-derived Chl-a maps from C2RCC altNN (or v2) for (a) Spring, (b) Summer and (c) Fall along British Columbia and Southeast Alaska.

processor (Brockmann et al., 2016). ADG443 is a combination of two components: organic detritus (non-pigmented) and gelbstoff (CDOM), which can be obtained independently by C2RCC. To do this, the forward in-water model uses different absorption spectral slopes for each component in the bio-optical modelling (Brockmann et al., 2016). Although the two products are defined independently by C2RCC, poor performance of the CDOM products was observed compared to ADG443 for our waters, which suggests that regional spectral slopes are needed to separate detritus from CDOM absorption (Bricaud et al., 2012; Mannino et al., 2014). Currently, the C2RCC altNN uses a CDOM slope of 0.025 nm⁻¹ as default, which is generally a high value and corresponds to the maximum value of CDOM slopes measured in the SoG, that varied from 0.016 to 0.025 nm⁻¹. This could be causing the poor performance of the CDOM (absorption by gelbstoff) retrieved from C2RCC for our waters. The ADG443 retrievals from the C2RCC altNN showed a better range of values for our waters than version 1. It is important to point out that one of the satellite-retrieved ADG443 values was an outlier (Fig. 4c), but no invalid flag or error was identified in the pixel window, and the value was therefore maintained, which likely contributed to the lower r-value for this model. Although the C2RCC v1 showed better performance in retrieving Rrs in the blue bands, as discussed above, this issue might have been compensated during CDOM retrievals by the extension of the NN ranges, since v1 was not comprising our expected range of values. The most recent version of SNAP (V 7.0) includes the extended alternative NN in the C2RCC local processing. Ultimately, the ADG443 achieved similar (or slightly better) CDOM retrievals than previous studies for other coastal areas. For instance, CDOM retrieval differences varied from 20.4 to 67.4% using different MODIS and SeaWiFS algorithms in the northeastern USA coast (Mannino et al., 2014) and about 70.0% for MERIS in the European seas (Zibordi et al., 2013).

4.2. Match-up data uncertainties

In situ measurements are considered the reference to which other data (e.g., satellite data) are generally compared. However, these may contain significant levels of uncertainty as a result of various sensor

inherent, experimental and environmental factors (Zibordi et al., 2012; Werdell et al., 2018; Vabson et al., 2019a, 2019b; Ruddick et al., 2019; Tilstone et al., 2020). In our dataset, comprising data mostly from the southern Strait of Georgia, a degree of spatial mismatch of water masses can be expected between the *in situ* and satellite samples due to the highly contrasted and temporally dynamic waters, especially at the interface between the Fraser River plume and ocean-influenced waters. Sampling points near the frontal region of the plume indicated this mismatch issue. This was minimized by using match up maps of surface currents (Halverson and Pawlowicz, 2016) to conservatively re-locate some samples (*i.e.*, allocate new coordinates) to the estimated location of the water mass at the time of the satellite passage. Only 4 points required re-location, as most of the data sampling was carried out during periods of slack water and low surface tidal currents. This approach slightly improved the performance of some match-up samples, but it is still difficult to quantify any remaining source of errors associated with this residual water mass mismatch. Overall, the spatial coefficients of variation from SAS-ST data corresponding to the match-up pixel-window varied from 2% to 17% (maximum values in the blue and red bands). For the satellite Rrs spatial variability within the extracted pixels, the median CV varied from 3 to 10% in the visible domain, indicating low variability.

Radiometric *in situ* measurements also have uncertainties due to instrument calibration, ship shadow and superstructure, environmental factors, and parametrization to address surface Fresnel reflection of the sky radiance (Mobley, 1999). Although we follow rigorous criteria for the acquisition of radiometric measurements with freshly calibrated instruments, acquisition only during solar noon and clear-sky days, and a set up to avoid shadow and ship superstructure (Mobley, 1999; Hooker and Morel, 2003; Wang and Costa, 2018), the comparison of results among studies must consider the expected variability and uncertainties among radiometers and protocols (Zibordi et al., 2012; Vabson et al., 2019a, 2019b; Ruddick et al., 2019). Inter-comparison of independent radiometric sensors showed that most of the variability in the field is related to the cosine response of the irradiance sensors, the field of view (or angular response), spatial non-uniformity of the targets (water and

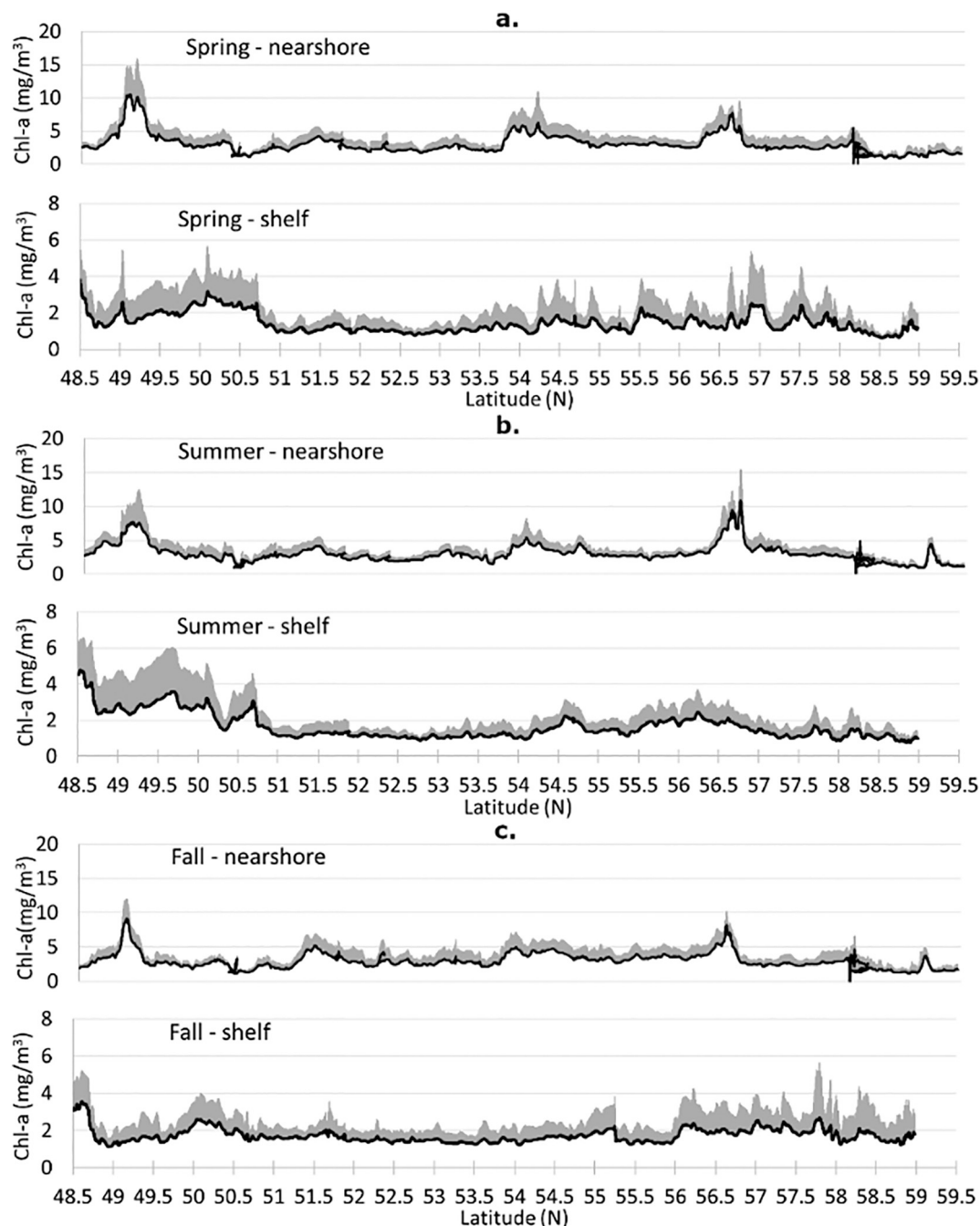


Fig. 13. Chl-a latitudinal distribution for (a) Spring, (b) Summer, and (c) Fall along nearshore and continental shelf transects in British Columbia and Southeast Alaska. Chl-a values are seasonal averages with positive standard deviations indicated by the gray area. Note different y-axis scales between nearshore and continental shelf plots.

sky) for the radiance measurements, and methods for data processing (Vabson et al., 2019b; Tilstone et al., 2020). The quantification of the uncertainties budget is hard to reach due to those dependent factors mentioned above (IOCCG, 2019), but they are an essential part of the agenda for fiducial reference measurements performed by several authors (e.g. Zibordi et al., 2012; Tilstone et al., 2020; Alikas et al., 2020). In the present study, the uncertainties budget (including Type A and Type B uncertainties; Alikas et al., 2020) were not computed. Providing fiducial reference measurements was not the objective of this analysis, but rather to evaluate the performance of the different OLCI processors in the study region. Previous studies have performed dedicated inter-comparison experiments to quantify uncertainties related to radiometric measurements with considerations to be used a fiducial reference

measurement (Tilstone et al., 2020). The authors computed the relative differences between sensors according to a reference measurement, including HyperSAS sensors. The differences in Rrs were on average within 3.5% at 443 nm, 1% at 560 nm, and 3% at 665 nm, with Ed accounting for the largest fraction of the variance in Rrs. In our study, data were acquired during solar noon and clear-sky conditions, which minimizes the uncertainties related to Ed and its propagation to Rrs measurements; however, the final uncertainty is still undetermined. For another series of sensors, Vabson et al. (2019b) also reported relative variability overall below 15% for radiance sensors, which includes 1% of uncertainty based on the laboratory experiment (Vabson et al., 2019a). It is important to highlight that those studies were performed in fixed platforms and well-controlled conditions.

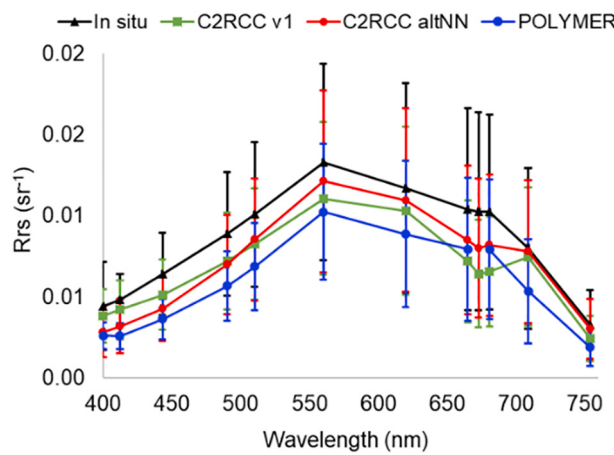


Fig. 14. Mean Rrs spectra for the *in situ* data and for each processor retrievals ($N = 25$). Error bars indicate ± 0.5 standard deviation.

Radiometric data are also influenced by the dependence on both viewing and illumination geometries, which can be reduced by corrections for the bidirectional effect (BRDF), i.e., the correction for non-nadir view and normalization for illumination conditions (Morel and Gentili, 1996). BRDF corrections are also affected by their associated uncertainties, especially in optically complex waters, and should be integrated into the overall budget for *in situ* and satellite data accuracy assessment (Talone et al., 2018; IOCCG, 2019). For the satellite retrievals, BRDF related uncertainties can be even larger for wide sensor zenith angles, as usually occurs at the edge of the image swath and large solar zenith angles (Zheng and DiGiocomo, 2017). Nonetheless, the evaluated processors in this study have different approaches regarding BRDF correction, i.e., C2RCC (SNAP processing and L2-OCNN) with no BRDF correction and POLYMER with BRDF correction (Park and Rudnick, 2005) (Section 2.3). Given the different approaches for the evaluated processors, our *in situ* Rrs was not BRDF corrected. Instead, to further understand POLYMER BRDF-corrected reflectance retrievals' performance, we performed an additional analysis by applying BRDF correction factors in our *in situ* Rrs based on the IOP model (Lee et al., 2011) reported by Talone et al. (2018). Based on a large AERONET_OC dataset, these authors computed correction factors varying from -8 to -12% from the blue to the red wavelengths for the Baltic Sea waters. Compared with our initial results (Table 1), the consideration of these factors showed improvement of POLYMER radiometric performance, resulting in a $BIAS_{Rrs}$ decrease of about 5 to 7% in the blue wavelengths, 8 to 11% in the green and 8 to 12% in the red. For the MdAPD, there was an overall improvement of about 1 to 8% across all wavelengths. These reduced $BIAS_{Rrs}$ and MdAPD, suggest similar POLYMER performance as C2RCC altNN (no BRDF correction, Table 1). It is important to highlight that C2RCC versions do not include a BRDF correction in the default processing. However, if an IOP-based BRDF model is applied for both C2RCC and *in situ* dataset, the improvement in the matchup statistics is expected to be similar to that observed here for POLYMER. This ultimately would not impact the choice of the algorithm used for Chl-a, TSM and CDOM retrievals. The application of a BRDF correction on the C2RCC reflectance data is available for Case 1 waters, but it is still under evaluation.

4.3. OLCI Sentinel-3 quality flags

The pixel-based quality flags recommended by the agencies and/or developers should be applied to guarantee the best quality of the satellite Level-2 dataset generated from different algorithms. The descriptions of scientific flags for ESA-L2 products are found in the OLCI Sentinel-3 User handbook (EUMETSAT, 2018), for C2RCC in Brockmann et al. (2016), and POLYMER in Steinmetz et al. (2016). For this

study, most of the recommended quality flags were used (see Section 2.3), but it is important to note that OLCI algorithms are evolving, and their products and quality control procedures are under constant evaluation. For instance, we observed that the C2RCC 'Out-of-Scope' flags (Rtosa_OOS and Rhow_OOS) had no impact on the match-up performance with pixels under this flag presenting good spectral quality. 'OOS' means the training dataset of the model does not recognize the retrieved spectra; however, the model can not simulate all possible water spectra. Thus, the use of this flag partially depends on the user's objective, and if the pre-defined flag thresholds are too strict, it may remove good pixels. This scenario occurred in our dataset, suggesting the need for future adjustments of the global settings applied for OLCI thresholds. For example, despite the good radiometric results found for pixels with the 'OOS' flags raised in the match-up analysis, the C2RCC altNN Level-3 images of the northern part of our study area revealed possible effects of adjacency in the first few pixels close to the coastline, coincident with the 'Rtosa-OOS' flag mask (Fig. 15a). This flag was then applied to the Level-3 composites to avoid this effect as the ADG(443) values were highly impacted (Fig. 15). According to Doerffer and Schiller (2007), the threshold to switch the warning flag on is difficult to define; consequently, the user is advised to check this flag carefully. In our case, we have not found degradation of the Rrs spectra and bio-physical retrievals, however, we opted to apply this flag to remove coastal adjacency, although this might be removing useful coastal data. In addition, for the NN-based products, a debatable issue is the use of pixels that raised the sunglint risk flag. Those pixels, which counted for half of our radiometric data, showed no degradation in the spectral quality and bio-physical match-up statistics. A larger dataset from this region, including approximately 700 *in situ* spectra, has shown the same feature (Wang, Z., unpublished data), suggesting that the sunglint-related flags should be further evaluated for OLCI data in turbid coastal waters, as it seems to be highly conservative.

For POLYMER, we applied most of the recommended flags in the match-up analysis, except the 'Thick Aerosol' flag. This flag seems to be erroneously raised in POLYMER version 4.9 for OLCI processing, warranting future studies (Steinmetz, personal communication). According to Steinmetz et al. (2016), the 'Inconsistency' flag should not invalidate the results, however, one of our Rrs match-up samples raised this flag and showed poor radiometry. Also, the Level-3 products showed that some of the pixels in clear waters with 'Inconsistency' flag exhibited invalid Rrs spectra. However, considering the Chl-a match-up data, 9 out of 95 samples had the 'Inconsistency' flag raised, but no particular Chla deviations related to this flag were observed. Conclusions about this flag are difficult to draw based on our limited data; thus, we opted not to invalidate those pixels as suggested by Steinmetz et al. (2016). Nonetheless, we recommend further radiometric validation and adjustments of this flag for OLCI Sentinel-3.

The POLYMER 'Case-2' flag, which is raised when the spectral optimization does not converge properly in highly scattering turbid waters, should also not invalidate the results. According to Steinmetz et al. (2016), the criterion to check for invalid convergence is that the estimated fitting parameters are within a reasonable range, and if not, a second optimization is performed considering more appropriate initial values for turbid waters. Although it is not an invalidating flag, in this study, we showed that pixels in which this flag was raised showed poor radiometric performance, strongly impacting Chl-a retrievals. This flag was therefore used to mask pixels out and improve Chl-a Level-3 products from POLYMER for BC waters, as discussed in the previous section.

4.4. Seasonal trends of TSM, CDOM and Chl-a retrievals from OLCI Sentinel-3A in the Northeast Pacific coastal waters

In order to further evaluate the application of OLCI Sentinel-3 products for BC and SEA, we compared the seasonal and latitudinal ranges of variability in TSM and Chl-a (from POLYMER), and CDOM (from C2RCC altNN) with those previously reported for different parts of

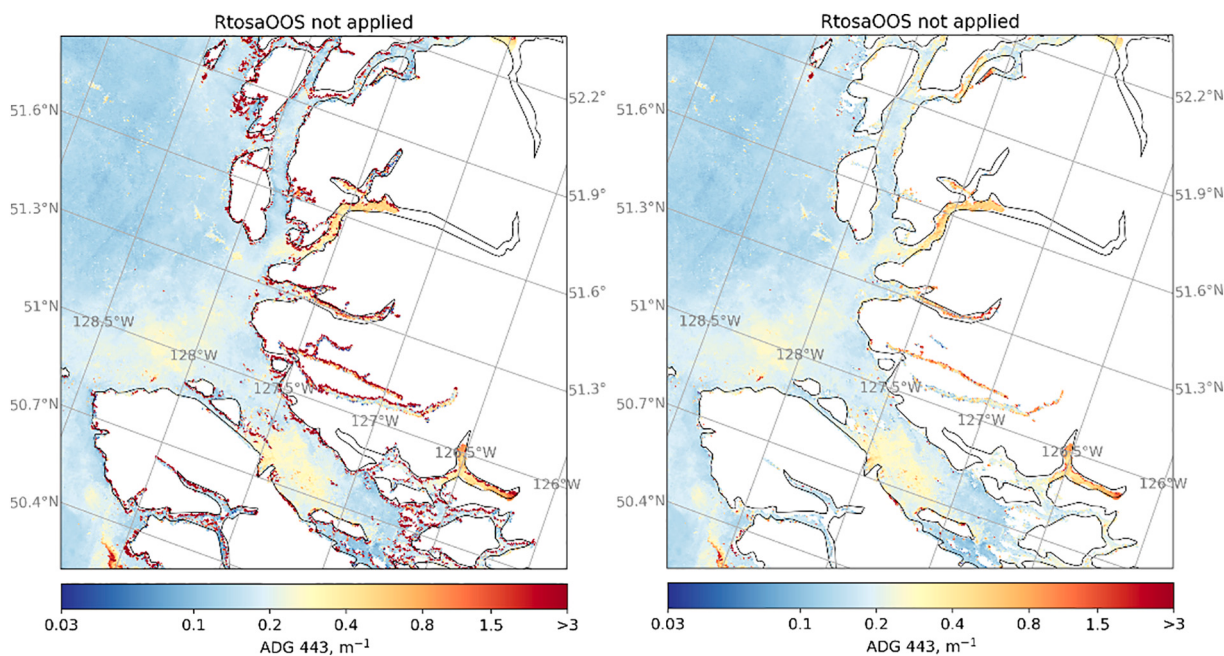


Fig. 15. Level-3 composite of ADG(443) for summer average (a) without removing pixels with the Rtosa_OOS flag and (b) after removing the pixels with the Rtosa_OOS flag. Note that the colormap is different from Fig. 10 to highlight the pixels with anomalous values close to the coast.

the coast, given that our *in situ* match-up dataset was mostly constrained to the southern BC coast. We are aware of the limitations of our Level-3 composites, which do not include the full OLCI Sentinel-3 dataset, and thus we limit our discussion to overall trends and assume the large standard deviations found for the seasonal averages represent the uncertainties of this analysis. Furthermore, a considerable limitation of our region is the cloud coverage. In the Salish Sea, corresponding to the southern part of our study area (47° to 51° N), the spatial coverage of chlorophyll data for the daily MODIS time series ranged from 10 to 40%, and the region sometimes has up to 12-day intervals between two images with full data coverage (Hilborn and Costa, 2018). In the case of Sentinel-3A daily coverage for our entire study area (47° to 59° N), the 4 km data available from the GlobColour Project (<http://www.globcolour.info/>) shows that the valid data coverage is generally between 5% and 35%, except for a few days when the data coverage is up to 50%. The valid data probability is expected to increase when using the original resolution data (300 m), as previously shown for MODIS-Aqua 1 km *versus* 250 m resolution data for the Gulf of Mexico (Feng et al., 2017). Globally, merging different sensors is an alternative to improve coverage, but previous studies have shown that valid daily data is not higher than 25% of the total ocean area (Gregg and Woodward, 1998; Maritorena et al., 2010). Given the scale of the study area and current application, we considered composites with $> 60\%$ cloud-free images to be an acceptable balance in terms of computational processing and data quality, maintaining the original resolution of the images. However, we recognize that future studies should include the full available OLCI dataset to generate robust conclusions about the local dynamics and bioregionalization studies.

Our nearshore TSM retrievals showed a well-defined seasonal pattern, with peaks reflecting the dynamics of the Fraser, Skeena and Nass rivers in BC, and Stikine and Alsek rivers in SEA, together comprising the major rivers discharging into the coastal waters of the northern Pacific Ocean (Whitney et al., 2005). The annual dynamics reflected the latitudinal gradient of seasonal snowmelt freshets and glacial melt flows (Morrison et al., 2012; Fleming et al., 2016; Fissel et al., 2017). In the Strait of Georgia, where most of TSM data from the literature is concentrated, the seasonal trends were well within the range of values reported (about 0.5 to 21.0 mg/L), linked to the dynamics of

the Fraser River (Loos and Costa, 2010; Phillips and Costa, 2017) and the phytoplankton bloom during Spring and Summer (Masson and Peña, 2009; Halverson and Pawlowicz, 2016; Phillips and Costa, 2017). Indeed, phytoplankton blooms in the SoG, with Chl-a concentrations up to 7.0 mg.m^{-3} , were previously related to high TSM, light attenuation and scattering (Phillips and Costa, 2017). In other coastal areas, the TSM dynamics were not coupled to Chl-a, suggesting a greater contribution of inorganic particles and terrestrial organic detritus. Along the continental shelf, larger TSM concentrations were observed during the summer on the west coast of Vancouver Island, where our data suggested that phytoplankton biomass was the largest component of the total suspended particles.

The CDOM retrievals along the coastal transect showed different seasonal and latitudinal patterns from TSM. A few of the observed CDOM peaks occurred in waters that did not exhibit large TSM loads, such as in the vicinity of Aristazabal and Banks Islands (52.5 to 53.7° N) in Summer and Fall (Fig. 11). In this region, CDOM concentration was higher than in northern waters influenced by the Nass and Skeena rivers, while the latter showed high TSM concentrations for the same season (Fig. 8). These trends require further investigation, but our dataset suggests contrasting small-scale processes between those regions. Within the SoG, CDOM values were similar to the ranges previously reported for this region (Komick et al., 2009; Phillips and Costa, 2017), where most of the available organic carbon is in the dissolved form, primarily produced by phytoplankton cells and, to a lesser extent, originated from the Fraser River discharged waters (Johannessen et al., 2003). In SEA, the Stikine River plume seems to be the most important contributor to CDOM in the region, except in the Fall when high CDOM was spread along the SEA coastal area and even occurred on the continental shelf. The northeast Pacific region contains numerous small catchments that discharge freshwater with high concentrations of dissolved organic carbon (DOC), suggesting that the dissolved carbon pool, which CDOM is part of, has a large allochthonous component (Oliver et al., 2017). Further research is required to investigate the nature of carbon pools in this region to better understand the fate of terrestrial material in coastal ocean food webs. Satellite-derived CDOM absorption provides useful proxies of aquatic DOC that can be applied to address these research questions (Vantrepotte et al., 2015; Ruescas et al., 2018).

Compared to the TSM and CDOM products, the deviations in the Chl-a match-ups were larger (Section 3.1), which could be reflected in higher inaccuracy on the Level-3 binned data. Thus, we recommend that the data should be used with caution, and standard deviations of the composed products must be highlighted. Nonetheless, the OLCI-derived Chl-a products showed the expected seasonal and local dynamics for this region. For instance, the spring and summer peaks in Chl-a (Fig. 12), typical for this region (e.g., Suchy et al., 2019; Carswell et al., 2017; Masson and Peña, 2009; Beamish and McFarlane, 2014; Jackson et al., 2015). A secondary phytoplankton bloom in the Fall is usually observed in BC coastal waters (Perry, 1984; Chandler et al., 2018; Suchy et al., 2019), and this was also detected by our data, especially near Calvert Island (51.5°) (Fig. 13c; nearshore). Also, in the SoG, which is under the influence of the Fraser River plume, the Sentinel-3A Chl-a values were similar to *in situ* data available in the literature (Stockner et al., 1979; Parsons et al., 1981; Masson and Peña, 2009; Komick et al., 2009; Loos and Costa, 2010; Phillips and Costa, 2017; Collins et al., 2009). These seasonal and local patterns are influenced by wind, temperature, available PAR (Allen and Wolfe, 2013; Suchy et al., 2019) and nutrient dynamics (Yin et al., 1995). At the regional scale, climate indices such as the Pacific Decadal Oscillation are correlated with Chl-a dynamics (Suchy et al., 2019).

For the water along the continental shelf, high Chl-a concentrations (up to $4.70 \pm 1.70 \text{ mg.m}^{-3}$) were observed on the west coast of Vancouver Island, corresponding to known bloom periods within the range of previously reported concentrations (Chandler et al., 2018). And, for this region, our data indicated that the phytoplankton bloom was the primary contributor to the relatively high TSM in this region. The west coast of Vancouver Island was the only section of the continental shelf transect where TSM made a significant contribution, although still below 1.0 mg/L. Overall, Summer and Fall Chl-a concentrations were higher along the SEA section of the shelf transect than along Central BC and the west coast of Haida Gwaii. Chl-a concentrations were particularly high at the east side of Baranof Island (57°N) in the Fall, with values over 2.0 mg.m^{-3} , expected in the region (Stabeno et al., 2016).

5. Conclusions

The rationale of the current work was to evaluate high resolution (300 m) satellite retrievals for a geomorphologically and oceanographically dynamic region that encompass optically complex waters. Sentinel-3 provides the necessary resolution for investigating such regions, and here we tested its application to the nearshore-terrestrial interface in the British Columbia and Southeast Alaska regions. Different approaches were tested to derive bio-physical products (Chl-a, TSM and CDOM) for the region of interest. First, the radiometric evaluation of the different processors showed that C2RCC v1 had the best performance when retrieving Rrs, primarily due to the best results in the blue bands. However, overall differences are still large (from 38 to 52% across wavelengths). The computation of specific vicarious calibration gains for C2RCC will improve its radiometric performance, and in the future, we expect that the alternative NN will be the most suitable approach for the study region due to the extended NN ranges. This was further supported by the better overall results obtained for ADG443 retrievals compared to version 1. POLYMER showed slightly poorer or similar radiometric results than C2RCC; however, improved results are expected with future validation considering *in situ* BRDF corrected data. It is important to note that the Rrs analysis presented here is limited regarding the number of match-up samples and the possible uncertainties associated with the *in situ* radiometric data. *In situ* radiometric data were acquired with freshly calibrated sensors, optimal geometry of acquisition, and only during clear sky days at solar noon.

Although POLYMER showed slightly inferior radiometric performance than C2RCC, the validation of biophysical products showed that Chl-a and TSM retrievals were the most accurate. This is likely a result of the improved integrity of the spectral shape in Rrs retrievals compared

to the NN models. Further, POLYMER showed broader applicability for the Northeast Pacific coastal waters since C2RCC algorithms would require region-specific tuning to improve retrievals of Chl-a and TSM from the inherent optical properties (IOPs). In our waters, the so-called ‘Case-2’ flag in POLYMER helped to significantly improve the Chl-a retrievals, removing pixels where high turbidity promoted poor Rrs retrievals, resulting in very low systematic bias (~1%), despite a still high percent difference (MdAD ~80%). Although not developed to be an excluding flag, the pixels where the ‘Case-2’ flag was raised were masked out for the Level-3 composites. Further, POLYMER provided technical advantages regarding processing time, being at least two times faster than C2RCC local processing, and also provided the largest number of valid data. With dedicated SVC gains for C2RCC and the use of the alternative NN (C2RCC v2) in the operational EUMETSAT Level-2 products, those processing-related advantages must be re-evaluated in balance with new match-ups validation. It is important to highlight that the current thresholds applied for some of the Level-2 quality flags, e.g. sunglint risk flag and C2RCC Rtsa OOS, are worth being revised for OLCI data in coastal waters.

After considering the observed relevant match-up differences and the application of quality flags that aim to reduce the errors, the seasonal and latitudinal trends of TSM, CDOM and Chl-a observed for BC and SEA demonstrated the validity of Sentinel-3A products in a large spatial scale, with values within the expected ranges in Northeast Pacific coastal waters. The satellite retrievals highlighted a few coastal trends, such as the association of small-scale variability with contrasting discharge dynamics along the coast and the decoupling of nearshore and continental shelf processes. This is particularly relevant to undersampled regions, such as the northern waters of the Northeast Pacific coast, where remotely sensed high-resolution data can provide insights that would otherwise not be possible. Our study has provided a framework with associated uncertainties and recommendations as a first step towards using Sentinel-3A to define and monitor the biogeochemical dynamics in complex coastal regions.

Funding

Fernanda Giannini was supported by a UBC/UVic Hakai Coastal Initiative postdoctoral fellowship. Fieldwork through the Hakai Institute was supported by the Tula Foundation. The project also had funds to Dr. Costa from NSERC NCE MEOPAR - Marine Environmental Observation, Prediction and Response Network; Canadian Space Agency (FAST 18FAVICB09); Canadian Foundation for Innovations (CFI); and NSERC Discovery Grant, Canada.

Description of author's responsibilities

Dr. Fernanda Giannini was responsible for the data collection and analysis and manuscript writing. Dr. Maycira Costa and Dr. Brian Hunt were responsible for the project conceptualization, results discussions and significant reviews in the manuscript. Dr. Derek Jacoby was responsible for setting up the high-performance computing and clouding system for the remote sensing data processing, also providing helpful edits in the text.

Declaration of Competing Interest

None.

Acknowledgments

We thank the staff of Hakai Institute and Department of Fisheries and Oceans, and personnel in the SPECTRAL Lab who participated in the *in situ* data sampling. We also express our gratitude to the BC Ferries crew for the logistical support during field sampling and the ONC (Ocean Networks Canada) for the technical support with the FOCOS (Ferry

Ocean Colour Observation Systems) data acquisition. The authors thank Msc Andrea Hilborn and Msc Bing Gao for optimizing part of the computational tools for the satellite validation analysis.

References

- Alikas, K., Ansko, I., Vabson, V., Ansper, A., Kangro, K., Uudeberg, K., 2020. Consistency of Radiometric Satellite Data over Lakes and Coastal Waters with Local Field Measurements. *Remote Sens.* 12, 616. <https://doi.org/10.3390/rs12040616>.
- Allen, S.E., Wolfe, M.A., 2013. Hindcast of the timing of the spring phytoplankton bloom in the strait of Georgia, 1968–2010. *Prog. Oceanogr.* 115, 6–13. <https://doi.org/10.1016/j.pocean.2013.05.026>.
- Babin, M., Stramski, D., Ferrari, G.M., Claustré, H., Bricaud, A., Obolensky, G., Hoepffner, N., 2003. Variations in the light absorption coefficients of phytoplankton, nonalgal particles, and dissolved organic matter in coastal waters around Europe. *J. Geophys. Res.* 108, 3211. <https://doi.org/10.1029/2001JC000882>.
- Bailey, S.W., Werdell, P.J., 2006. A multi-sensor approach for the on-orbit validation of ocean color satellite data products. *Remote Sens. Environ.* 102, 12–23. <https://doi.org/10.1016/j.rse.2006.01.015>.
- Beamish, R.J., and McFarlane, G.A., 2014. *The sea among us: The amazing strait of Georgia*. Harbour Publishing, British Columbia, Canada.
- Behrenfeld, M.J., O'Malley, R.T., Siegel, D. a, McClain, C.R., Sarmiento, J.L., Feldman, G. C., Milligan, A.J., Falkowski, P.G., Letelier, R.M., Boss, E.S., 2006. Climate-driven trends in contemporary ocean productivity. *Nature* 444, 752–755. <https://doi.org/10.1038/nature05317>.
- Behrenfeld, M.J., O'Malley, R.T., Boss, E.S., Westberry, T.K., Graff, J.R., Halsey, K.H., Milligan, A.J., Siegel, D.A., Brown, M.B., 2016. Revaluating Ocean warming impacts on global phytoplankton. *Nat. Clim. Chang.* 6, 323–330. <https://doi.org/10.1038/nclimate2838>.
- Boss, E., Picheral, M., Leeuw, T., Chase, A., Karsenti, E., Gorsky, G., Taylor, L., Slade, W., Ras, J., Claustré, H., 2013. The characteristics of particulate absorption, scattering and attenuation coefficients in the surface ocean; contribution of the Tara oceans expedition. *Methods Oceanogr.* 7, 52–62. <https://doi.org/10.1016/j.mio.2013.11.002>.
- Bricaud, A., Morel, A., Prieur, L., 1981. Absorption by dissolved organic matter of the sea (yellow substance) in the UV and visible domains. *Limnol. Oceanogr.* 26, 43–53. <https://doi.org/10.4319/lo.1981.26.1.0043>.
- Bricaud, A., Claustré, H., Ras, J., Oubelkheir, K., 2004. Natural variability of phytoplanktonic absorption in oceanic waters: influence of the size structure of algal populations. *J. Geophys. Res.* 109, 1–12. <https://doi.org/10.1029/2004JC002419>.
- Bricaud, A., Ciotti, A.M., Gentili, B., 2012. Spatial-temporal variations in phytoplankton size and colored detrital matter absorption at global and regional scales, as derived from twelve years of SeaWiFS data (1998–2009). *Glob. Biogeochem. Cycles* 26. <https://doi.org/10.1029/2010GB003952>.
- Brockmann, C., Doerffer, R., Peters, M., Stelzer, K., Sabine, E., Ana, 2016. Evolution of the C2RC Neural Network for Sentinel 2 and 3 for the retrieval of ocean colour products in normal and extreme optically complex waters. In: *Living Planet Symposium 2016*. Prague, Czech Republic.
- Carswell, T., Costa, M., Young, E., Komick, N., Gower, J., Sweeting, R., 2017. Evaluation of MODIS-aqua atmospheric correction and chlorophyll products of western north American coastal waters based on 13 years of data. *Remote Sens.* 9, 1–24. <https://doi.org/10.3390/rs9101063>.
- State of the physical, biological and selected fishery resources of Pacific Canadian marine ecosystems in 2017. In: Chandler, P.C., King, S.A., Boldt, J. (Eds.), 2018. *Can. Tech. Rep. Fish. Aquat. Sci.* 3266, p. 245 viii +.
- Ciotti, A.M., Lewis, M.R., Cullen, J.J., 2002. Assessment of the relationships between dominant cell size in natural phytoplankton communities and the spectral shape of the absorption coefficient. *Limnol. Oceanogr.* 47, 404–417.
- Collins, A.K., Allen, S.E., Pawlowicz, R., 2009. The role of wind in determining the timing of the spring bloom in the strait of Georgia. *Can. J. Fish. Aquat. Sci.* 66, 1597–1616. <https://doi.org/10.1139/F09-071>.
- Doerffer, R., Schiller, H., 2007. The MERIS case 2 water algorithm. *Int. J. Remote Sens.* 28, 517–535. <https://doi.org/10.1080/01431160600821127>.
- Doerffer, R., Schiller, H., 2008. MERIS Regional Coastal and Lake Case 2 Water Project - Atmospheric Correction ATBD. GKSS Research Center 21502 Geesthacht Version 1.0. 18. May 2008.
- Dogliotti, A.I., Ruddick, K.G., Nechad, B., Doxaran, D., Knaeps, E., 2015. A single algorithm to retrieve turbidity from remotely-sensed data in all coastal and estuarine waters. *Remote Sens. Environ.* 156, 157–168. <https://doi.org/10.1016/j.rse.2014.09.020>.
- Donlon, C., Berruti, B., Mecklenberg, S., Nieke, J., Rebhan, H., Klein, U., Buongiorno, A., Mavrocordatos, C., Frerick, J., Seitz, B., Goryl, P., Femenias, P., Stroede, J., Sciarra, R., 2012. The Sentinel-3 mission: Overview and status. *Int. Geosci. Remote Sens. Symp.* 1711–1714. <https://doi.org/10.1109/IGARSS.2012.6351194>.
- Dutkiewicz, S., Hickman, A.E., Jahn, O., Henson, S., Beaufieu, C., Monier, E., 2019. Ocean colour signature of climate change. *Nat. Commun.* 10 <https://doi.org/10.1038/s41467-019-08457-x>.
- EUMETSAT, 2017. Requirements for Copernicus OC-VCAL infrastructure. In: REF: SOLVO/EUM/16/VCA/D8. ISSUE: 1.3. July 2017.
- EUMETSAT, 2018. Sentinel-3 OLCI Marine User Handbook. Doc.No.: EUM/OPS-SEN3/MAN/17/907205. July 2018. Darmstadt, Germany.
- Feng, L., Hu, C., Barnes, B.B., Mannino, A., Heidinger, A.K., Strabala, K., Iraci, L.T., 2017. Cloud and sun-glint statistics derived from GOES and MODIS observations over the intra-Americas sea for GEO-CAPE mission planning. *J. Geophys. Res.* 122, 1725–1745. <https://doi.org/10.1002/2016JD025372>.
- Fissel, D.B., Lin, Y., Scoon, A., Lim, J., Brown, L., Clouston, R., 2017. The variability of the sediment plume and ocean circulation features of the Nass River estuary, British Columbia. *Satell. Oceanogr. Meteorol.* 2 <https://doi.org/10.18063/som.v2i2.316>.
- Fleming, S.W., Hood, E., Dahlke, H.E., O'Neil, S., 2016. Seasonal flows of international British Columbia-Alaska rivers: the nonlinear influence of ocean-atmosphere circulation patterns. *Adv. Water Resour.* 87, 42–55. <https://doi.org/10.1016/j.advwatres.2015.10.007>.
- Giannini, F., Garcia, C.A.E., Tavano, V.M., Ciotti, A.M., 2013. Effects of low-salinity and high-turbidity waters on empirical ocean colour algorithms: an example for southwestern Atlantic waters. *Cont. Shelf Res.* 59, 84–96. <https://doi.org/10.1016/j.csr.2013.04.013>.
- Gordon, H.R., Wang, M., 1994. Retrieval of water-leaving radiance and aerosol optical thickness over the oceans with SeaWiFS: a preliminary algorithm. *Appl. Opt.* 33, 443. <https://doi.org/10.1364/ao.33.000443>.
- Gossen, J.I., Ruddick, K.G., Dogliotti, A.I., 2019. Atmospheric correction of OLCI imagery over extremely turbid waters based on the red, NIR and 1016 nm bands and a new baseline residual technique. *Remote Sens.* 11 (1–24) <https://doi.org/10.3390/rs11030220>.
- Goyens, C., Jamet, C., Schroeder, T., 2013. Evaluation of four atmospheric correction algorithms for MODIS-aqua images over contrasted coastal waters. *Remote Sens. Environ.* 131, 63–75. <https://doi.org/10.1016/j.rse.2012.12.006>.
- Gregg, W.W., Woodward, R.H., 1998. Improvements in coverage frequency of ocean color: combining data from SeaWiFS and MODIS. *IEEE Trans. Geosci. Remote Sens.* 36, 1350–1353. <https://doi.org/10.1109/36.701084>.
- Groom, S., Sathyendranath, S., Ban, Y., Bernard, S., Brewin, R., Brodas, V., Brockmann, C., Chauhan, P., Choi, J., Chuprin, A., Ciavatta, S., Cipollini, P., Donlon, C., Franz, B., He, X., Hirata, T., Jackson, T., Kampel, M., Krasemann, H., Lavender, S., Pardo-Martinez, S., Mélin, F., Platt, T., Santoleri, R., Skakala, J., Schaeffer, B., Smith, M., Steinmetz, F., Valente, A., Wang, M., 2019. Satellite Ocean colour: current status and future perspective. *Front. Mar. Sci.* 6 <https://doi.org/10.3389/fmars.2019.00485>.
- Halverson, M., Pawlowicz, R., 2016. Tide, wind, and river forcing of the surface currents in the Fraser river plume. *Atmosphere-Ocean* 54, 131–152. <https://doi.org/10.1080/07055900.2016.1138927>.
- Hieronymi, M., Müller, D., Doerffer, R., 2017. The OLCI neural network swarm (ONNS): a bio-geo-optical algorithm for open ocean and coastal waters. *Front. Mar. Sci.* 4, 1–18. <https://doi.org/10.3389/fmars.2017.00140>.
- Hilborn, A., Costa, M., 2018. Applications of DINEOF to satellite-derived chlorophyll-a from a productive coastal region. *Remote Sens.* 10, 1449 <https://doi.org/10.3390/rs10091449>.
- Holm-Hansen, O., Lorenzen, C.J., Holmes, R.W., Strickland, J.D.H., 1965. Fluorometric determination of chlorophyll. *ICES J. Mar. Sci.* 30, 3–15. <https://doi.org/10.1093/icesjms/30.1.3>.
- Hooker, S.B., Morel, A., 2003. Platform and environmental effects on above-water determinations of water-leaving radiances. *J. Atmos. Ocean. Technol.* 20, 187–205. [https://doi.org/10.1175/1520-0426\(2003\)020<0187:PAEEOA>2.0.CO;2](https://doi.org/10.1175/1520-0426(2003)020<0187:PAEEOA>2.0.CO;2).
- IOCCG, 2000. Remote Sensing of Ocean Colour in Coastal, and Other Optically-Complex, Waters. In: Sathyendranath, S. (Ed.), Reports of the International Ocean-Colour Coordinating Group, No. 3. IOCCG, Dartmouth, Canada.
- IOCCG, 2019. Uncertainties in Ocean Colour Remote Sensing. In: Mélin, F. (Ed.), IOCCG Report Series, No. 18. International Ocean Colour Coordinating Group, Dartmouth, Canada. <https://doi.org/10.25607/OPB-696>.
- Jackson, J.M., Thomson, R.E., Brown, L., Willis, P.G., Borstad, G.A., 2015. Satellite chlorophyll off the British Columbia coast, 1997–2010. *J. Geophys. Res. Ocean.* 120 <https://doi.org/10.1002/2014JC010496>, 4709–4728.
- Johannessen, S.C., Macdonald, R.W., Paton, D.W., 2003. A sediment and organic carbon budget for the greater strait of Georgia. *Estuar. Coast. Shelf Sci.* 56, 845–860. [https://doi.org/10.1016/S0272-7714\(02\)00303-7](https://doi.org/10.1016/S0272-7714(02)00303-7).
- Johannessen, S.C., Masson, D., Macdonald, R.W., 2006. Distribution and cycling of suspended particles inferred from transmissivity in the strait of Georgia, Haro Strait and Juan de Fuca Strait. *Atmosphere-Ocean* 44, 17–27. <https://doi.org/10.3137/ao.440102>.
- Komick, N.M., Costa, M.P.F., Gower, J., 2009. Bio-optical algorithm evaluation for MODIS for western Canada coastal waters: an exploratory approach using in situ reflectance. *Remote Sens. Environ.* 113, 794–804. <https://doi.org/10.1016/j.rse.2008.12.005>.
- Kyryliuk, D., Kratzer, S., 2019. Evaluation of sentinel-3A OLCI products derived using the case-2 regional coastcolour processor over the Baltic Sea. *Sensors (Switzerland)* 19. <https://doi.org/10.3390/s19163609>.
- Lavender, S., Jackson, T., Sathyendranath, S., 2015. The Ocean Colour Climate Change Initiative: Merging ocean colour observations seamlessly. *Ocean Chall.* 21, 29–31.
- Lee, Z.P., Du, K., Voss, K.J., Zibordi, G., Lubac, B., Arnone, R., Weidemann, A., 2011. An inherent-optical-property-centered approach to correct the angular effects in water-leaving radiance. *Appl. Opt.* 50, 3155–3167. <https://doi.org/10.1364/AO.50.003155>.
- Loos, E.A., Costa, M., 2010. Inherent optical properties and optical mass classification of the waters of the strait of Georgia, British Columbia. *Canada. Prog. Oceanogr.* 87, 144–156. <https://doi.org/10.1016/j.pocean.2010.09.004>.
- Loos, E., Costa, M., Johannessen, S., 2017. Underwater optical environment in the coastal waters of British Columbia, Canada. *Facets* 2, 872–891. <https://doi.org/10.1139/facets-2017-0074>.
- Lyu, H., Wang, Q., Wu, C., Zhu, L., Li, Y., Huang, J., 2015. Variations in optical scattering and backscattering by organic and inorganic particulates in Chinese lakes of Taihu,

- Chaochu and Dianchi. Chin. Geogr. Sci. 25, 26–38. <https://doi.org/10.1007/s11769-014-0689-y>.
- Malick, M.J., Cox, S.P., Mueter, F.J., Peterman, R.M., 2015. Linking phytoplankton phenology to salmon productivity along a north-south gradient in the Northeast Pacific Ocean. Can. J. Fish. Aquat. Sci. 72, 697–708. <https://doi.org/10.1139/cjfas-2014-0298>.
- Mannino, A., Novak, M.G., Hooker, S.B., Hyde, K., Aurin, D., 2014. Algorithm development and validation of CDOM properties for estuarine and continental shelf waters along the northeastern U.S. Coast. Remote Sens. Environ. 152, 576–602. <https://doi.org/10.1016/j.rse.2014.06.027>.
- Maritorena, S., d'Andon, O.H.F., Mangin, A., Siegel, D.A., 2010. Merged satellite ocean color data products using a bio-optical model: characteristics, benefits and issues. Remote Sens. Environ. 114, 1791–1804. <https://doi.org/10.1016/j.rse.2010.04.002>.
- Masson, D., Peña, A., 2009. Chlorophyll distribution in a temperate estuary: the strait of Georgia and Juan de Fuca Strait. Estuar. Coast. Shelf Sci. 82, 19–28. <https://doi.org/10.1016/j.ecss.2008.12.022>.
- McClain, C.R., 2009. A decade of Satellite Ocean color observations. Annu. Rev. Mar. Sci. 1, 19–42. <https://doi.org/10.1146/annurev.marine.010908.163650>.
- McNicol, G., Bulmer, C., D'Amore, D., Sanborn, P., Saunders, S., Giesbrecht, I., Arriola, S. G., Bidlack, A., Butman, D., Buma, B., 2019. Large, climate-sensitive soil carbon stocks mapped with pedology-informed machine learning in the North Pacific coastal temperate rainforest. Environ. Res. Lett. 14 <https://doi.org/10.1088/1748-9326/aed52>.
- Mélin, F., Vantrepotte, V., Clerici, M., D'Alimonte, D., Zibordi, G., Berthon, J.F., Canutti, E., 2011. Multi-sensor satellite time series of optical properties and chlorophyll-a concentration in the Adriatic Sea. Prog. Oceanogr. 91, 229–244. <https://doi.org/10.1016/j.pocean.2010.12.001>.
- Mitchell, B.G., Kahru, M., Wieland, J., Stramska, M., 2002. Determination of spectral absorption coefficients of particles, dissolved material and phytoplankton for discrete water samples. In: Ocean Optics Protocols for Satellite Ocean Color Sensor Validation, Revision, 3, pp. 231–257.
- Mobley, C.D., 1994. Light and Water: Radiative Transfer in Natural Waters. Academic Press, London, p. 592.
- Mobley, C.D., 1999. Estimation of the remote-sensing reflectance from above-surface measurements. Appl. Opt. 38, 7442. <https://doi.org/10.1364/ao.38.007442>.
- Mograne, M., Jamet, C., Loisel, H., Vantrepotte, V., Mériaux, X., Cauvin, A., 2019. Evaluation of five atmospheric correction algorithms over French optically-complex waters for the sentinel-3A OLCI Ocean color sensor. Remote Sens. 11, 668. <https://doi.org/10.3390/rs11060668>.
- Moore, G.F., Aiken, J., Lavender, S.J., 1999. The atmospheric correction of water colour and the quantitative retrieval of suspended particulate matter in case II waters: application to MERIS. Int. J. Remote Sens. 20, 1713–1733. <https://doi.org/10.1080/014311699212434>.
- Morel, A., Bricaud, A., 1981. Theoretical results concerning the optics of phytoplankton, with special reference to remote sensing applications. Oceanogr. From Sp. https://doi.org/10.1007/978-1-4613-3315-9_35.
- Morel, A., Gentili, B., 1996. Diffuse reflectance of oceanic waters III implication of bidirectionality for the remote-sensing problem. Appl. Opt. 35, 4850. <https://doi.org/10.1364/ao.35.004850>.
- Morel, A., Maritorena, S., 2001. Bio-optical properties of oceanic waters: a reappraisal. J. Geophys. Res. Ocean. 106, 7163–7180. <https://doi.org/10.1029/2000jc000319>.
- Morel, A., Huot, Y., Gentili, B., Werdell, P.J., Hooker, S.B., Franz, B.A., 2007. Examining the consistency of products derived from various ocean color sensors in open ocean (case 1) waters in the perspective of a multi-sensor approach. Remote Sens. Environ. 111, 69–88. <https://doi.org/10.1016/j.rse.2007.03.012>.
- Morrison, J., Foreman, M.G.G., Masson, D., 2012. A method for estimating monthly freshwater discharge affecting British Columbia coastal waters. Atmosphere-Ocean 50, 1–8. <https://doi.org/10.1080/07055900.2011.637667>.
- Nechad, B., Ruddick, K.G., Park, Y., 2010. Calibration and validation of a generic multisensor algorithm for mapping of total suspended matter in turbid waters. Remote Sens. Environ. 114, 854–866. <https://doi.org/10.1016/j.rse.2009.11.022>.
- Nelson, N.B., Siegel, D.A., 2013. The global distribution and dynamics of Chromophoric dissolved organic matter. Annu. Rev. Mar. Sci. 5, 447–476. <https://doi.org/10.1146/annurev-marine-120710-100751>.
- Neukermans, G., Ruddick, K., Loisel, H., Roose, P., 2012. Optimization and quality control of suspended particulate matter concentration measurement using turbidity measurements. Limnol. Oceanogr. Methods 10, 1011–1023. <https://doi.org/10.4319/lom.2012.10.1011>.
- Oliver, A.A., Tank, S.E., Giesbrecht, I., Korver, M.C., Floyd, W.C., Sanborn, P., Bulmer, C., Lertzman, K.P., 2017. A global hotspot for dissolved organic carbon in hypermaritime watersheds of coastal British Columbia. Biogeosciences 14, 3743–3762. <https://doi.org/10.5194/bg-14-3743-2017>.
- O'Neil, S., Hood, E., Bidlack, A.L., Fleming, S.W., Arimitsu, M.L., Arendt, A., Burgess, E., Sergeant, C.J., Beaudreau, A.H., Timm, K., Hayward, G.D., Reynolds, J.H., Pyare, S., 2015. Icefield-to-ocean linkages across the northern pacific coastal temperate rainforest ecosystem. Bioscience 65, 499–512. <https://doi.org/10.1093/biosci/biv027>.
- O'Reilly, J.E., et al., 2000. In: Hooker, S.B., Firestone, E.R. (Eds.), SeaWiFS Post-launch calibration and validation analyses, part 3. NASA Tech. Memo. 2000–206892, Vol. 11. NASA Goddard Space Flight Center, p. 49.
- Park, Y.J., Ruddick, K., 2005. Model of remote-sensing reflectance including bidirectional effects for case 1 and case 2 waters. Appl. Opt. 44, 1236–1249. <https://doi.org/10.1364/AO.44.001236>.
- Parsons, T., Stronach, J., Borstad, G., Louttit, G., Perry, R., 1981. Biological fronts in the strait of Georgia, British Columbia, and their relation to recent measurements of primary productivity. Mar. Ecol. Prog. Ser. 6, 237–242. <https://doi.org/10.3354/meps006237>.
- Pawlowicz, R., 2017. Seasonal cycles, hypoxia, and renewal in a Coastal Fjord (Barkley sound, British Columbia). Atmosphere-Ocean 55, 264–283. <https://doi.org/10.1080/07055900.2017.1374240>.
- Pearlman, S.R., Costa, H.S., Jung, R.A., McKeown, J.J., Pearson, H.E., 1995. Solids (section 2540). pp. 2–53–2–64. In: Eaton, A.D., Clesceri, L.S., Greenberg, A.E. (Eds.), Standard Methods for the Examination of Water and Wastewater. American Publ. Health Assoc.
- Pereira-Sandoval, M., Ruescas, A., Urrego, P., Ruiz-Verdú, A., Delegido, J., Tenjo, C., Soria-Perpinà, X., Vicente, E., Soria, J., Moreno, J., 2019. Evaluation of atmospheric correction algorithms over spanish inland waters for sentinel-2 multi spectral imagery data. Remote Sens. 11, 1–23. <https://doi.org/10.3390/rs11121469>.
- Perry, R.I., 1984. Plankton Blooms of the British Columbia Northern Shelf: Seasonal Distributions and Mechanisms Influencing their Formation. University of British Columbia, Faculty of Graduate Studies – Zoology, p. 239.
- Phillips, S.R., Costa, M., 2017. Spatial-temporal bio-optical classification of dynamic semi-estuarine waters in western North America. Estuar. Coast. Shelf Sci. 199, 35–48. <https://doi.org/10.1016/j.ecss.2017.09.029>.
- Pinckney, J.L., 2010. The Fourth SeaWiFS HPLC Analysis Round-Robin Experiment (SeaHARRE-4). In: Hooker, S.B., Thomas, C.S., Van Heukelem, L., Schlüter, L., Russ, M.E., Ras, J., Pinckney, J.L. (Eds.), NASA Tech. Memo - The Fourth SeaWiFS HPLC Analysis Round-Robin Experiment (SeaHARRE-4).
- Prieur, L., Sathyendranath, S., 1981. An optical classification of coastal and oceanic waters based on the specific spectral absorption curves of phytoplankton pigments, dissolved organic matter, and other particulate materials. Limnol. Oceanogr. 26, 671–689. <https://doi.org/10.4319/lo.1981.26.4.0671>.
- Röttgers, R., Heymann, K., Krasemann, H., 2014. Suspended matter concentrations in coastal waters: methodological improvements to quantify individual measurement uncertainty. Estuar. Coast. Shelf Sci. 151, 148–155. <https://doi.org/10.1016/j.ecss.2014.10.010>.
- Royer, T.C., 1982. Coastal fresh water discharge in the Northeast Pacific. J. Geophys. Res. 87, 2017–2021. <https://doi.org/10.1029/JC087IC03p02017>.
- Ruddick, K.G., Ovidio, F., Rijkeboer, M., 2000. Atmospheric correction of sea WiFS imagery for turbid coastal and inland waters. Appl. Opt. 39, 897–912.
- Ruddick, K.G., Voss, K., Boss, E., Castagna, A., Frouin, R., Gilerson, A., Hieronymi, M., Carol Johnson, B., Kuusk, J., Lee, Z., Ondrusek, M., Vabson, V., Vendt, R., 2019. A review of protocols for fiducial reference measurements of water-leaving radiance for validation of satellite remote-sensing data over water. Remote Sens. 11, 2198. <https://doi.org/10.3390/rs11192198>.
- Ruescas, A.B., Hieronymi, M., Mateo-Garcia, G., Koponen, S., Kallio, K., Camps-Valls, G., 2018. Machine learning regression approaches for colored dissolved organic matter (CDOM) retrieval with S2-MSI and S3-OLCI simulated data. Remote Sens. 10, 1–25. <https://doi.org/10.3390/rs10050786>.
- Sathyendranath, S., Brewin, R.J.W., Jackson, T., Mélin, F., Platt, T., 2017. Ocean-colour products for climate-change studies: what are their ideal characteristics? Remote Sens. Environ. 203, 125–138. <https://doi.org/10.1016/j.rse.2017.04.017>.
- Seegers, B.N., Stumpf, R.P., Schaeffer, B.A., Loftin, K.A., Werdell, P.J., 2018. Performance metrics for the assessment of satellite data products: an ocean color case study. Opt. Express 26, 7404. <https://doi.org/10.1364/oe.26.007404>.
- Siegel, D.A., Wang, M., Maritorena, S., Robinson, W., 2000. Atmospheric correction of satellite ocean color imagery: the black pixel assumption. Appl. Opt. 39, 3582. <https://doi.org/10.1364/ao.39.003582>.
- Stabeno, P.J., Bond, N.A., Kachel, N.B., Ladd, C., Mordy, C.W., Strom, S.L., 2016. Southeast Alaskan shelf from southern tip of Baranof Island to Kayak Island: currents, mixing and chlorophyll-a. Deep. Res. Part II Top. Stud. Oceanogr. 132, 6–23. <https://doi.org/10.1016/j.dsr2.2015.06.018>.
- Stavn, R.H., Rick, H.J., Falster, A.V., 2009. Correcting the errors from variable sea salt retention and water of hydration in loss on ignition analysis: implications for studies of estuarine and coastal waters. Estuar. Coast. Shelf Sci. 81, 575–582. <https://doi.org/10.1016/j.ecss.2008.12.017>.
- Steinmetz, F., Deschamps, P.-Y., Ramon, D., 2011. Atmospheric correction in presence of sun glint: application to MERIS. Opt. Express 19, 9783. <https://doi.org/10.1364/oe.19.009783>.
- Steinmetz, F., Ramon, D., Deschamps, P.Y., 2016. ATBD v1 - Polymer Atmospheric Correction Algorithm ref: D2.3 Date: 23/12/2016 Issue: 2.1. PML, United Kingdom.
- Stockner, J.G., Cliff, D.D., Shortreed, K.R.S., 1979. Phytoplankton ecology of the strait of Georgia, British Columbia. J. Fish. Res. Board Can. 36, 657–666. <https://doi.org/10.1139/f79-095>.
- Suchy, K.D., Le Baron, N., Hilborn, A., Perry, R.I., Costa, M., 2019. Influence of environmental drivers on spatio-temporal dynamics of satellite-derived chlorophyll a in the strait of Georgia. Prog. Oceanogr. 176, 102134. <https://doi.org/10.1016/j.pocean.2019.102134>.
- Talone, M., Zibordi, G., Lee, Z., 2018. Correction for the non-nadir viewing geometry of AERONET-OC above water radiometry data: an estimate of uncertainties. Opt. Express 26, A541. <https://doi.org/10.1364/oe.26.00a541>.
- Thomson, R.E., 1981. Oceanography of the British Columbia coast. Can. Spec. Publ. Fish. Aquat. Sci. 56, 291.
- Tilstone, G., Mallor-Hoya, S., Gohin, F., Couto, A.B., Sá, C., Goela, P., Cristina, S., Airs, R., Icely, J., Zühlke, M., Groom, S., 2017. Which ocean colour algorithm for MERIS in north west European waters? Remote Sens. Environ. 189, 132–151. <https://doi.org/10.1016/j.rse.2016.11.012>.
- Tilstone, G., Dall'Olmo, G., Hieronymi, M., Ruddick, K., Beck, M., Ligi, M., Costa, M., D'Alimonte, D., Vellucci, V., Vansteenvagen, D., Bracher, A., Wiegmann, S., Kuusk, J., Vabson, V., Ansko, I., Vendt, R., Donlon, C., Casal, T., 2020. Field

- intercomparison of radiometer measurements for ocean colour validation. *Remote Sens.* 12, 1–53. <https://doi.org/10.3390/rs12101587>.
- Vabson, V., Kuusk, J., Ansko, I., Vendt, R., Alikas, K., Ruddick, K., Ansper, A., Bresciani, M., Burmester, H., Costa, M., D'Alimonte, D., Dall'Olmo, G., Damiri, B., Dinter, T., Giardino, C., Kangro, K., Ligi, M., Paavel, B., Tilstone, G., Van Dommelen, R., Wiegmann, S., Bracher, A., Donlon, C., Casal, T., 2019a. Laboratory intercomparison of radiometers used for satellite validation in the 400–900 nm range. *Remote Sens.* 11, 1101. <https://doi.org/10.3390/rs11091129>.
- Vabson, V., Kuusk, J., Ansko, I., Vendt, R., Alikas, K., Ruddick, K., Ansper, A., Bresciani, M., Burmester, H., Costa, M., D'Alimonte, D., Dall'Olmo, G., Damiri, B., Dinter, T., Giardino, C., Kangro, K., Ligi, M., Paavel, B., Tilstone, G., Van Dommelen, R., Wiegmann, S., Bracher, A., Donlon, C., Casal, T., 2019b. Field intercomparison of radiometers used for satellite validation in the 400–900 nm range. *Remote Sens.* 11, 1129. <https://doi.org/10.3390/rs11091129>.
- Vandenberg, N., Costa, M., Coady, Y., Agbaje, T., 2017. PySciDON: A python scientific framework for development of ocean network applications. In: 2017 IEEE Pacific Rim Conf. Commun. Comput. Signal Process. PACRIM 2017 - Proc. 2017-Janua, 1–6. <https://doi.org/10.1109/PACRIM.2017.8121926>.
- Vantrepotte, V., Danhiez, F.-P., Loisel, H., Oullion, S., Mériaux, X., Cauvin, A., Dessailly, D., 2015. CDOM-DOC relationship in contrasted coastal waters: implication for DOC retrieval from ocean color remote sensing observation. *Opt. Express* 23, 33. <https://doi.org/10.1364/oe.23.000033>.
- Wang, Z., Costa, M., 2018. Autonomous shipborne *in situ* reflectance data in optically complex coastal waters for validation of Sentinel-3 imagery: A case study of the Salish Sea, Canada. In: Proceedings of the XXIV Ocean Optics Conference. Dubrovnik, Croatia. Oct 2018.
- Wang, M., Shi, W., 2005. Estimation of ocean contribution at the MODIS near-infrared wavelengths along the east coast of the U.S.: two case studies. *Geophys. Res. Lett.* 32, 1–5. <https://doi.org/10.1029/2005GL022917>.
- Ware, D.M., Thomson, R.E., 2005. Bottom-up ecosystem trophic dynamics determine fish production in the Northeast Pacific. *Science*. 308, 1280–1284. <https://doi.org/10.1126/science.1109049>.
- Warren, M.A., Simis, S.G.H., Martinez-Vicente, V., Poser, K., Bresciani, M., Alikas, K., Spyarakos, E., Giardino, C., Ansper, A., 2019. Assessment of atmospheric correction algorithms for the sentinel-2A MultiSpectral imager over coastal and inland waters. *Remote Sens. Environ.* 225, 267–289. <https://doi.org/10.1016/j.rse.2019.03.018>.
- Werdell, P.J., McKenna, L.I.W., Boss, E., Ackleson, S.G., Craig, S.E., Gregg, W.W., Lee, Z., Maritorena, S., Roessler, C.S., Rousseaux, C.S., Stramski, D., Sullivan, J.M., Twardowski, M.S., Tzortziou, M., Zhang, X., 2018. An overview of approaches and challenges for retrieving marine inherent optical properties from ocean color remote sensing. *Prog. Oceanogr.* 160, 186–212. <https://doi.org/10.1016/j.pocean.2018.01.001>.
- Whitney, F.A., Crawford, W.R., Harrison, P.J., 2005. Physical processes that enhance nutrient transport and primary productivity in the coastal and open ocean of the subarctic NE Pacific. *Deep. Res. Part II Top. Stud. Oceanogr.* 52, 681–706. <https://doi.org/10.1016/j.dsr2.2004.12.023>.
- Yin, K., Harrison, P.J., Pond, S., Beamish, R.J., 1995. Entrainment of nitrate in the Fraser river estuary and its biological implications: II. Effects of spring vs. neap tides and river discharge. *Estuar. Coast. Shelf Sci.* 40, 529–544. <https://doi.org/10.1006/ecss.1995.0036>.
- Zhang, M., Hu, C., Cannizzaro, J., English, D., Barnes, B.B., Carlson, P., Yarbro, L., 2018. Comparison of two atmospheric correction approaches applied to MODIS measurements over north American waters. *Remote Sens. Environ.* 216, 442–455. <https://doi.org/10.1016/j.rse.2018.07.012>.
- Zheng, G., DiGiocomo, P.M., 2017. Uncertainties and applications of satellite-derived coastal water quality products. *Prog. Oceanogr.* 159, 45–72. <https://doi.org/10.1016/j.pocean.2017.08.007>.
- Zibordi, G., Ruddick, K., Ansko, I., Moore, G., Kratzer, S., Icely, J., Reinart, A., 2012. In situ determination of the remote sensing reflectance: an inter-comparison. *Ocean Sci.* 8, 567–586. <https://doi.org/10.5194/os-8-567-2012>.
- Zibordi, G., Mélin, F., Berthon, J.F., Canutti, E., 2013. Assessment of MERIS Ocean color data products for European seas. *Ocean Sci.* 9, 521–533. <https://doi.org/10.5194/os-9-521-2013>.
- Zibordi, G., Melin, F., Berthon, J.F., 2018. A regional assessment of OLCI data products. *IEEE Geosci. Remote Sens. Lett.* 15, 1490–1494. <https://doi.org/10.1109/LGRS.2018.2849329>.